**Background Simulation and Verification for DM-Ice**

By

Bethany Reilly

A dissertation submitted in partial fulfillment of
the requirements for the degree of

Doctor of Philosophy

(Physics)

at the
UNIVERSITY OF WISCONSIN–MADISON
2014

Date of final oral examination: July 30, 2014

The dissertation is approved by the following members of the Final Oral Committee:
Reina Maruyama, Assistant Professor, Yale University, Physics
Albrecht Karle, Professor, University of Wisconsin-Madison, Physics
Lisa Everett, Associate Professor, University of Wisconsin-Madison, Physics
Peter Timbie, Professor, University of Wisconsin-Madison, Physics
Rosemary Russ, Assistant Professor, University of Wisconsin-Madison, Curriculum and Instruction

# BACKGROUND SIMULATION AND VERIFICATION FOR DM-ICE

Bethany Reilly

Under the supervision of Professor Albrecht Karle

At the University of Wisconsin-Madison

The search for dark matter is motivated by measurements that show there exists approximately five times more dark matter than the ordinary (baryonic) matter which has been the focus of scientific study since the dawn of science. The field of direct dark matter searches is an exciting one, with many different experiments performing their searches with different target materials and experimental methods. Their results have also varied, leading to a great deal of tension and uncertainty as to the characteristics of dark matter and our understanding of the low energy behavior of certain materials. Some experiments have seen hints of a dark matter signal, only to later determine their results consistent with expected backgrounds. Only one experiment, DAMA/LIBRA, claims a dark matter discovery; this stands out starkly in the field due to the strong exclusion limits measured by other experiments. It would be a giant step forward if we were able to resolve the tension between DAMA and the rest of the direct detection experiments.

DM-Ice is an experiment designed for a direct detection search for dark matter. Using a NaI(Tl) target, DM-Ice searches for WIMP (weakly interacting massive particles) dark matter via scintillation associated with nuclear recoil in the crystal, which is then observed by PMTs. DM-Ice can test the DAMA/LIBRA result, using the same target material while running in the Southern Hemisphere. The DM-Ice prototype runs at the South Pole station, deployed underneath the IceCube Neutrino Observatory. This thesis describes the simulation work performed in order to understand the prototype detector, DM-Ice17.

Dark matter background, evidence, and current understanding are discussed by way of introduction to the field. Description and discussion of detection methods and current experimental dark matter detection results follows.

The DM-Ice detector itself is then considered in detail, in terms of motivation, design, and function. The assembly, deployment and operation of DM-Ice17 is also discussed.

The purpose of simulating the radioactive backgrounds present in the DM-Ice17 detector is to understand the detector and the contamination levels present in each of its components, and to provide information needed for design and material selection for the full-scale DM-Ice detector. The Geant4 simulation toolkit was used to simulate the detector. The simulation is described in terms of geometry, particle decay and propagation, and producing an energy spectrum. This simulated energy spectrum was then used to characterize the detector, and this process is described as well.

Future work in simulation for DM-Ice is then discussed, as well as future plans for the experiment as a whole.

This thesis demonstrates that the simulation I have created aligns well with the data from DM-Ice17. This simulation allows insight into and verification of the radioactive contamination of each of the component of the detector, as well as that of its surroundings. The simulation also allows for detailed consideration of the contamination levels in different materials, which is needed in order to select materials and designs for the full-scale DM-Ice detector. Details regarding contributions of different isotopes in each region of the detector to the region of interest (low-energy; $\sim$ 0-10 keV) are extracted from the simulation, which allows optimization of understanding what degree of cleanliness is needed for purposes of our dark matter search.

DM-ICE

# ACKNOWLEDGMENTS

I would like to thank first of all my advisor, Reina Maruyama. Your patience and diligence in guiding me on my PhD journey has been greatly appreciated. I am grateful to have had an advisor who has high standards for her students, and maintains a good balance between being helpful and available and also allowing students time to figure things out on their own. Thank you for taking me on; I'm proud to have been your first graduate student, and am sure that every student you mentor will benefit greatly from your guidance.

Thank you so much, Albrecht, for stepping in to serve as my advisor of record. Our discussions have been very helpful.

I also want to thank Lisa Everett, Peter Timbie, and Rosemary Russ - you have each contributed to my graduate experience and education in important ways, and I'm delighted to have you on my committee. Thank you for your investment in me, it has been greatly appreciated.

Next I have to thank my fellow graduate students; Walter, Antonia, and Zack, it's been a blast. We've worked hard, sat through endless meetings, wrestled through deciding whether a particular result made sense, and had grand times out at the terrace or unwinding at dinner after a day of conference talks. Matt, it's been great to have you join us as well! I've learned so much from each of you, and enjoyed our time together building this great experiment. Thanks for the great memories.

To my lunch buddies, it's been such a blast! You all are the friendships that framed my grad school experience. I have loved the fun, the silliness, and the serious talks. I look forward to keeping in touch as we go on to the next steps, and will treasure the time we had together these past years. I absolutely love that I am a part of a group dubbed "the four Musketeers."

Andrea, what can I say. Who knew when I sat down next to some other girls that first day of orientation that I'd be meeting such a wonderful person who would become one of my closest friends. You're an absolutely wonderful person, and I'm so thankful that we've grown this relationship together. You also brought Jim around, who I am so glad is now like a brother to me, as you are like a sister. You two are such a blessing to me. Enjoy Canada, and I'll come visit if at all possible, but come back as close as you can when you settle long term, won't you?!

Kenny...when I first knew you, I just knew you were the one who knew all kinds of physics, and was still a good explainer. I didn't really get to know you for quite a while, but I knew early on you were a good guy. Little did I know how much wonderful time we'd spend together over the years! I can't explain how glad I am that we are friends. I've never had a truly close friend who was a guy, so you are unique thus far in that regard to me. I think of you like the older brother I never had.

Will, I don't think I've ever had a close friend more different from me. But we agree on the important things - like which dog breeds are the best, and that dessert should be eaten often. Seriously though, I've really appreciated

getting to know how you think about things. Your logical and generous nature is a combination that I wouldn't have guessed, and contributes so much to our gatherings. We've had so much fun together, and I'm so glad we got put in the same office and became friends.

Tova, we had a great few years there. Thanks for sharing those times with us. I wish you all the best.

Becca and Dana, at first you were just extensions of Kenny and Will, but I'm so glad that we have gone so far past that point. I have so enjoyed hanging out with you both. Becca, you are such an awesome person, and you and Kenny are such a sweet couple. I so look forward to keeping in touch with both of you over the years. Dana, you're a crazy person, and you're pretty awesome. I'm so happy to have your particular brand of silliness in my life. Bring Will back to Wisconsin in the end, will you? :)

Megan, who knew that Megthany would journey so far together. I was so grateful to have such a faithful friend and classmate at Taylor, and I held my breath as you decided on a grad school. I couldn't be happier that you joined me here, and we've had these years together! There's been a lot of great pies, real talks, and life changes. I'm so happy that you and Alex have found each other. You are both awesome, and I love you both. Thank you too for your faithful help with India, and for the times you've imitated her; you have a gift!

Laura. I come to you not first in the list, but first in my heart. You're my anchor, my steady support. You're the one that I fight with and say what I think, knowing that we'll always be close even if I make you mad. We remind each other of our past, and of our dreams. You've also given me a brother in law, and a share in your three children. Eric, Fierna, and Owen, you have each brought so much love into my heart and my life. I so look forward to watching you grow up and find your own places in the world. I can't wait to see what you do to change it. All my love to you all: Laura, Matt, and kids.

Kevin and Matthew, my dear brothers. It's been harder for me to keep in touch with you during these college and grad school years, but I hope you know how much I love each of you. You both inspire me, and I'm so proud of each of you. May we find more time to spend together as time goes on.

Tiffany and Jenny, you have both been such blessings to me! I'm so grateful I've gotten to have you for my new sisters. We've had many fun times, some serious talks, and I look forward to more of those as the years go on.

Auntie Boo, you've been so much to me my whole life. I'm so grateful for your steady presence and encouragement without fail. There is no way I would be writing this thesis without you. Uncle Greg, Nate, Nick, and Luke - thank you all for everything. Boys, I'm so grateful to you for squeezing into one room the year I lived with you. I'm so glad that you are now more like brothers than cousins to me. I love you all dearly, and am so proud of who you are growing up to be.

Dad and Barb, thanks for your encouragement and support.

Steph. It's such a special blessing to have a friend from such an early age, and beyond any reasonable gift to have one like you. We've been through thick and thin, and our friendship has survived the tests of time and distance, only growing stronger over time. Your constant presence in my life is a pillar that keeps me standing upright. The love we have is so precious. You are such a wonderful, lovely person, and I am beyond grateful for our friendship. Words don't cut it.

Dr. Kiers, I had never even thought of going to graduate school until you mentioned it one time. I thank you so much for your guidance, and perhaps even more, your faith in me. I wouldn't have dared to apply without your

encouragement, and your belief that I was up to the challenge. These years in grad school have been wonderful ones, and in many ways I owe them all to you. Thank you so much. And I want to say again how much I appreciated your dedication to your teaching. The best learning experiences of my life have been in your classes, and as I begin to teach, your standard of teaching excellence is the one I will strive for.

Lisa, I wanted to say a few words about how much your support has meant throughout grad school. I realized early on that you were rooting for all of our success, and wanted to give us the information we needed to make that happen. I learned so much about how to "do" grad school from you, and my whole class has been so appreciative of your guidance and encouragement. When in doubt, one of the primary resources we trust has been to "go ask Lisa." Thank you so much for everything.

There are so many who have encouraged me and contributed to my life throughout the years. Thank you to Leslie, and Jess, and Vin, and Emily B., and Kim, and Dalia, and Cali, and Michelle, and Evan, and Kerry - my early years would not have been the same without you! And thank you to Lynne, Sarah "Richter," Hillary, Emily R., Slucas, Becca, Kflo, Mimi, Roxxi, Jessica, and everyone else who did life with me on 1st North. They were great years, and I'm grateful for the contributions each of you made to my life. And to Kristi, one of my few lasting non-wing friends - I loved that you let me tag along so much, it was a blast. :) Nicki, doing Wicked remains one of my most awesome memories from college - thanks for going out on a limb with me! Jennie, our meals together were so special. I also want to my grad school physics class - we were big, we were friendly, and we had so many awesome times. May Thanksphysicsgiving and Chanakwanaphysmas live forever in our hearts, and not least our most epic Holiday Colloquium ever. Einstein Ringers, we had an awesome run! I've had the pleasure to get to know some wonderful Madison folk in the last few years through my debut into the world of performing musical theater. Special thanks to Carla, Grace, Ann, Bill, Cherry, Emily, Simone, Katie, Janine, Sharon, Matt, Frost, Winter, and everyone else who has made my theater experiences such a wonderful addition to my life.

For those whose names I've (presumably inevitably) inadvertently left off, please forgive me, and know that I am grateful for you! It's been a long and busy summer, and my brain is a bit fried. Thank you to each of you!

And to all my friends and family, I would have never survived graduate school without your support! Thank you for thinking through research problems with me, helping me move, hanging out and playing board games when I needed to de-stress, and (you know who you are) "uh-huh"ing your way through listening to me ramble about things that make no sense to you. I appreciate every one of you.

Finally, I wish to dedicate this thesis to my mother. Mom, you dedicated your life to your kids, and we reaped the benefits without question while we were young. I realized as I grew that I had a special mom, and I was grateful. I was a shy kid, but that wasn't why I always wanted to bring friends to play at my house instead of theirs - it was because my mom was awesome, and I loved to be nearby. You taught me everything I needed to know about life, including how to have fun, how to cope with an imperfect past, how to work hard, how to love people, and how to give of oneself for the sake of others. You didn't teach me any fancy cooking, or how to put on makeup, but you gave me what I needed to survive and prosper in life. You gave me my siblings, and my first dear animal friends. You gave me a foundation on which I have built everything else. I love you and miss you, the curly-haired tooth fairy who burps like a lamb. Thank you for giving me absolutely everything.

# TABLE OF CONTENTS

Page

Page

# LIST OF TABLES

Table Page

# LIST OF FIGURES

Figure Page

Figure Page

Figure Page

Figure Page

# Chapter 1

# Introduction

Dark matter makes up nearly 27% of the universe; only about 5% is understood at present (the baryonic matter) [1]. The effects of dark matter have been seen through a variety of astronomical observations (see section 2.1). Cosmology provides a great deal of information relevant to understanding dark matter, and provides a means for creating feasible dark matter theories. Given testable theories, we can perform dark matter searches. DM-Ice is a new dark matter experiment which will provide a unique perspective on the dark matter search. My work is to understand and model the backgrounds which are present in DM-Ice. This is key since dark matter detection is a low-signal, rare event search. We need to understand the backgrounds in order to interpret the data from our prototype, DM-Ice17, and in order to devise the best design and materials purity requirements for the full scale DM-Ice.

Chapter 1 of this thesis consists of this introductory section. Chapter 2 discusses evidence for the existence of dark matter, and goes through some of what we know or guess about dark matter, which guides our experimental searches.

Chapter 3 discusses the state of tension in which we find the dark matter detection field at this time. Many direct detection experiments are reporting results, but only one group reports a definite signal. This group is DAMA, a NaI target experiment located in the Gran Sasso underground laboratory in Italy. DAMA claims a dark matter discovery at the level of 11 $\sigma$, but while other experiments have seen hints of a dark matter signal, none have

confirmed DAMA's signal. In fact, many dark matter experiments have ruled out the phase space (mass and cross section) of the dark matter DAMA claims to see. DM-Ice seeks to resolve this tension once and for all, by essentially replicating the DAMA experiment in the Southern Hemisphere in order to improve background vs. signal discernment. Further detail regarding the DM-Ice experiment is found in Chapter 4.

Chapter 5 introduces the Geant4 background simulation created for DM-Ice; Chapter 6 discusses comparison between data from DM-Ice17 and the DM-Ice17 simulation, and what we gain from this comparison. Chapter 7 is a brief discussion of the upcoming work to be done for the experiment, and Chapter 8 summarizes conclusions and results of the simulation.

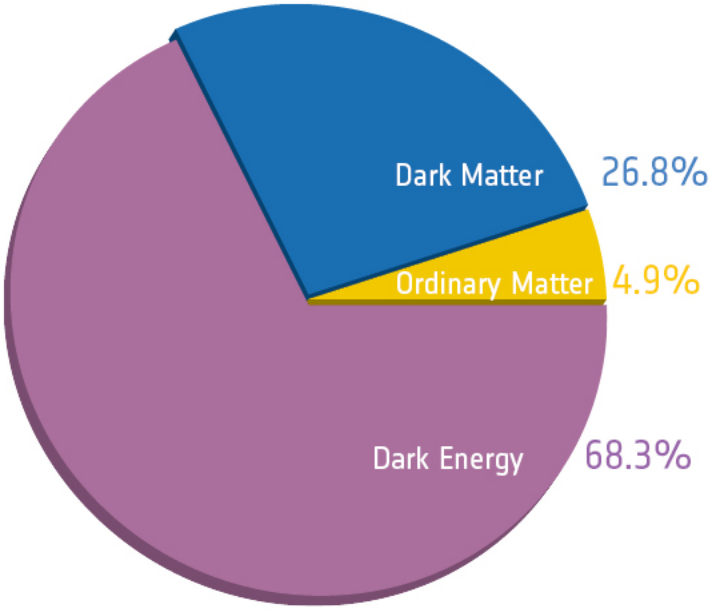


Figure 1.1: Distribution of "stuff" in the universe, based on measurements of the cosmic microwave background by the Planck space telescope [1]. Recall $E = mc^2$, so mass and energy are effectively equivalent.

DM-ICE

# Chapter 2

# Dark Matter

## 2.1 Evidence for Dark Matter

Dark matter has been a topic of scientific consideration for more than eighty years, and the evidence of the existence of dark matter is now extremely strong. This evidence comes from both astronomy and cosmology, and is quite varied. Most of the evidence of highest significance is discussed in this chapter.

### 2.1.1 Galaxy Clusters: First evidence

Jan Oort first postulated dark matter in 1932, which he thought was present in the disk of the Milky Way. This was later found to be based on erroneous assumptions, but was quickly followed by Fritz Zwicky's observations of the Coma cluster. Zwicky's measurements were the first indications of dark matter as we understand it today (1933). Zwicky measured the gravitational mass of the Coma cluster by the virial theorem, and the luminous mass by observations of the stars. The discrepancy between these results gave the first real evidence for the presence of dark matter in galaxy clusters.

### 2.1.2 Galaxy Rotation Curves

The speed at which spiral galaxies rotate has provided a means to detect the presence of dark matter. The rotation speed of objects in spiral galaxies can be measured by considering the Doppler shifting of spectral lines. By Newton's second law and the law of gravitation,

we know that (Equation 2.1)

$$F_{centripetal} = ma_{centripetal} = \frac{mv^2}{r} = \frac{GmM}{r^2} \tag{2.1}$$

Therefore for a mass which depends on galactic radius r, $v^2(r) = \frac{FM(r)}{r}$. By this reasoning we expect that v(r) for r greater than the radius of the visible disc of a galaxy should fall off as $\frac{1}{\sqrt{r}}$. Measurements (see Figure 2.1) show, however, that the rotation speed remains steady beyond the visible disc, indicating the presence of invisible matter. This matter forms an additional halo of the galaxy, with a density proportional to $\frac{1}{r^2}$.

When we consider the mass-to-light ratio M/L, this ratio becomes exceedingly high beyond the visible portion of the galaxy disk; in some cases in the thousands or higher. M/L is standardized according to the mass and light of the Sun; M/L = 1 represents the Sun. Thus M/L less than one implies high brightness relative to mass, and M/L greater than one implies low brightness relative to mass. The high M/L values agree well with the proposed dark matter model, since M/L ratios above order 10 can't be explained well by luminous matter (this statement is valid only when considering the joint M/L ratio of an entire galaxy; individual stars can have M/L ratios that are quite high, but stars of this sort are not common enough to explain what we see).

The observation of galaxy rotation curves began rather simply; Zwicky was able to observe the Coma cluster by using optical telescopes. When radiotelescopes became available, it became possible to observe the 21 cm spectral line of neutral hydrogen. Observing this line out beyond the optical disk of a galaxy allows the measurement of rotation curves in this region. The flat rotation curves within the optical disk may possibly be explained by regular matter, but the behavior of the rotation curves beyond the optical disk is a significant evidence for dark matter. [11]

### 2.1.3 Gravitational Lensing

Gravitational lensing occurs when light is deflected around a cluster of dark matter by general relativistic factors. Strong lensing is based only on gravitational optics theory, and only probes matter inside a small region. Weak lensing modifies the shape of all sources, and

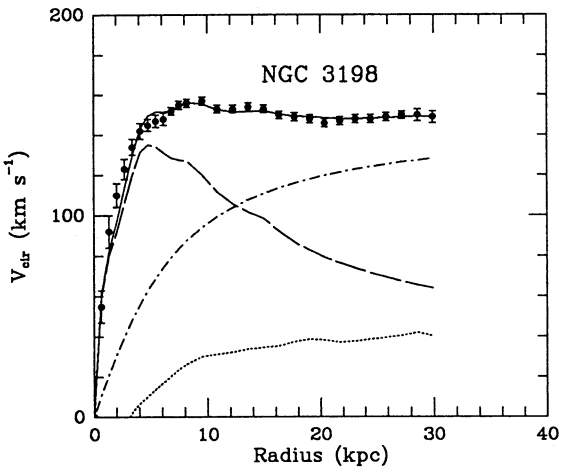


Figure 2.1: Galaxy rotation curves provide evidence for missing matter based on the rotation rates of galaxies. Here is the rotation curve measured for spiral galaxy NGC 3198. The top line is observed speed. The dashed line is the speeds we would expect for visible matter. The dotted line is gases, and the dash-dotted line is the dark halo. [6]

changes the ellipticity of galaxies. Strong and weak lensing together can probe structural and dynamical properties of dark haloes in all regions, and predictions of cosmological models can be tested. Strong and weak lensing provide almost direct probes of matter and gravity over physical scales between 1 kpc and 100 Mpc.

#### 2.1.3.1 Strong gravitational lensing

Strong lensing can estimate mass content of objects or regions; this gives evidence for dark matter by gravitational lensing. What is actually calculated is the mass-to-light ratio (M/L). Strong lensing produces distortions of galaxies which are significant enough to be visible by the eye on telescope images. Weak lensing is much more common but more difficult to detect. Strong lensing is relatively rare since it requires a very massive galaxy cluster between Earth and the lensed object, and galaxy clusters of this size are not terribly common. Strong gravitational lensing is also differentiated from weak lensing by forming multiple images from the "lens." Presuming that general relativity is valid, galaxies are

dominated by dark matter, judging from the measured mass-to-light ratios from strong lensing. M/L ratio increases with mass and radius. The light and matter distributions are not misaligned. Galaxies are observed fairly well via strong lensing, but in order to achieve similar results for clusters of galaxies, weak lensing must be used.

#### 2.1.3.2 Weak gravitational lensing

Weak lensing is observed by measuring the shape and orientation of sets of galaxies in proximity to one another. The effects are significantly reduced in comparison to strong lensing, as one expects, but careful analysis still yields a great deal of useful knowledge. Reconstruction of weak lensing effects is a well-developed technique, and is limited by observational or other limited knowledge rather than anything inherent to the method.

#### 2.1.3.3 Microlensing

Microlensing reveals that Cold Dark Objects or MaCHOs (such as black holes) have a mass fraction of $< 0.1$. (i.e., the mass allowed for MaCHOs is too small to explain dark matter) MaCHOs are Massive Compact Halo Objects; they are baryonic matter but radiate very little light. Gravitational lensing can occur when one star passes behind another, causing the more distant star to appear brighter due to the lensing effect. Microlensing occurs when the nearer star has a planet in orbit which lines up with the distant star. This also causes a brightening of the distant star, but more faintly due to the small mass of the planet relative to its star. The ruling out of MaCHOs has been extremely significant in the search to discover the identity of dark matter; focus largely shifted to WIMPs after the MaCHOs fell from favor.

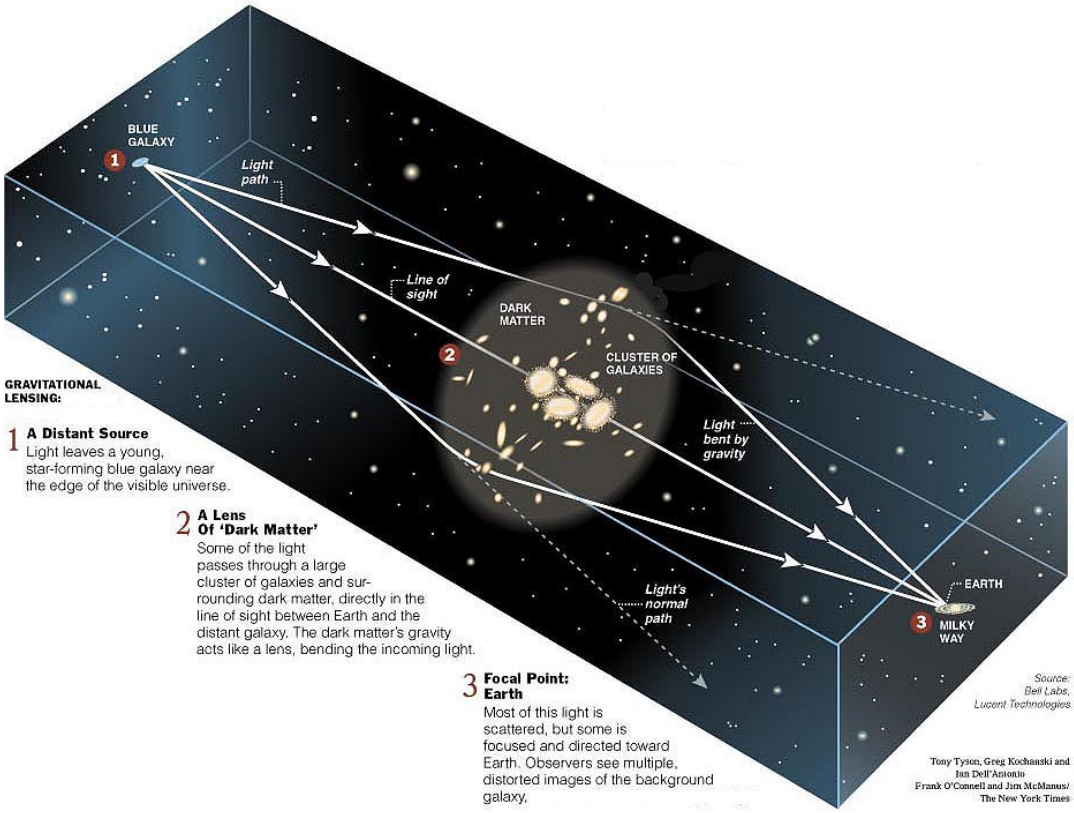


Figure 2.2: Gravitational lensing involves light from distant sources being bent by the gravity of objects between the source and observers on Earth. The degree of bending can be reconstructed from the light received at Earth, and can then be used itself to infer the amount of mass needed to produce that result. Evidence of non-visible matter based on these methods is therefore another handle on dark matter. This image depicts strong lensing.

Credit: Tony Tyson, Greg Kochanski and Ian DellAntonio; Frank OConnell and Jim McManus, adopted from The New York Times [7].

#### 2.1.3.4 Bullet Cluster

The Bullet Cluster provides perhaps the most striking evidence for dark matter, as it involves the collision of two galaxy clusters and has an interesting and beautiful image to show. There are three types of observational tools used here. An optical telescope, an X-ray telescope (Chandra) and gravitational lensing. The pink is the X-ray observations, the blue is the lensing, and the stars are optical (visible) images. The clumping of the gas at the center of the collision between the two galaxy clusters, since gas interacts with other gas particles. The dark matter is inferred to be in the blue region; since it interacts very seldom (if ever), the dark matter of one galaxy cluster may pass through the other cluster's dark matter without slowing down. The bullet cluster image combines weak and strong lensing mass reconstructions. Found are two massive substructures, offset with Chandra's baryon distribution, observed by X-rays. The bullet and lensing cluster observations give a dark matter cross section limit. Conservative upper limits from collisionless dark matter give cross section divided by matter is less than 1.25 (for bullet cluster) or 4 (for lensing cluster) $cm^2$/gram

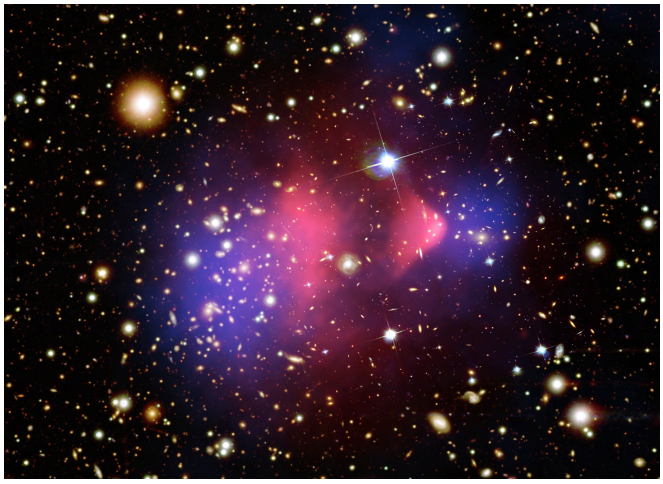

Figure 2.3: The "Bullet Cluster" collision observation provides evidence of the existence of dark matter. Two galaxy clusters collided/passed through each other, and the interaction (or non-interaction) between the two galaxy clusters is what is of interest. In the image, it can be seen that the pink regions appear to have interacted with each other, and slowed down. The blue regions have become separated from each other, as though they passed through without interacting. The behavior of the pink region is consistent with x-ray emitting hot gas, and the blue region is consistent with non-interacting dark matter. The pink has been superimposed on the optical image (white/yellow, stars) by observation of x-rays, and the blue regions have been inferred from the effects of gravitational lensing. [7]

### 2.1.4 Planck

The Planck space telescope [1] measures the Cosmic Microwave Background in impressive detail. The map's variations are due to the interactions of the CMB with various objects in the universe (which change the intensity detected) before being detected by the probe. This map of the CMB allows us to calculate the $\Omega_b$, the baryonic fraction of the universe (how much baryonic matter there is of all the "stuff" in the universe). Note: $\Omega_i$ is defined as a relative density, equal to $\rho_i/\rho_{crit}$, where $\rho_{crit}$ is the density required for a flat universe.

Planck measures $\Omega_b h^2 = 0.02207 \pm 0.00033$ [1], where h is the reduced Hubble constant, $\mathrm{h} = \frac{H_0}{100(km/s)/Mpc} = 0.719$ [12]. This gives 4.9% baryonic matter in the universe. Planck values for a few more key variables are reproduced in table 2.1.

| **Parameter** | Mass Fraction |
|---|---|
| $\Omega_\Lambda$ | 0.683 |
| $\Omega_b$ | 0.049 |
| $\Omega_c$ | 0.268 |
| $\Omega_b h^2$ | 0.022 |
| $\Omega_c h^2$ | 0.12 |

Table 2.1: Planck ΛCDM parameter measurements [1]

| Parameter | Definition |
|---|---|
| $\omega_\mathrm{b} \equiv \Omega_\mathrm{b} h^2$ . . . . . | Baryon density today |
| $\omega_\mathrm{c} \equiv \Omega_\mathrm{c} h^2$ . . . . . | Cold dark matter density today |
| $100\theta_\mathrm{MC}$ . . . . . | $100\times$ approximation to $r_*/D_\mathrm{A}$ (used in CosmoMC) |
| $\tau$ . . . . . | Thomson scattering optical depth due to reionization |
| $\Omega_K$ . . . . . | Curvature parameter today with $\Omega_\mathrm{tot} = 1 - \Omega_K$ |
| $Y_\mathrm{P}$ . . . . . | Fraction of baryonic mass in helium |
| $n_\mathrm{s}$ . . . . . | Scalar spectrum power-law index ($k_0 = 0.05$ Mpc$^{-1}$) |
| $\ln(10^{10} A_\mathrm{s})$ . . . . . | Log power of the primordial curvature perturbations ($k_0 = 0.05$ Mpc$^{-1}$) |
| $\Omega_\Lambda$ . . . . . | Dark energy density divided by the critical density today |
| Age . . . . . | Age of the Universe today (in Gyr) |
| $\Omega_\mathrm{m}$ . . . . . | Matter density (inc. massive neutrinos) today divided by the critical density |
| $z_\mathrm{re}$ . . . . . | Redshift at which Universe is half reionized |
| $H_0$ . . . . . | Current expansion rate in km s$^{-1}$Mpc$^{-1}$ |

Figure 2.4: Useful definitions from Planck [1]

## Planck and MaCHOs

Why do we expect dark matter to be non-baryonic? Could quarks combine to form some sort of matter that could explain the effects we ascribe to dark matter? MaCHOs (Massive Compact Halo Objects) were a valid theory for dark matter for a time (comparisons between the names "MaCHOs" and "WIMPs" are excellent). However, Planck calculates the mass

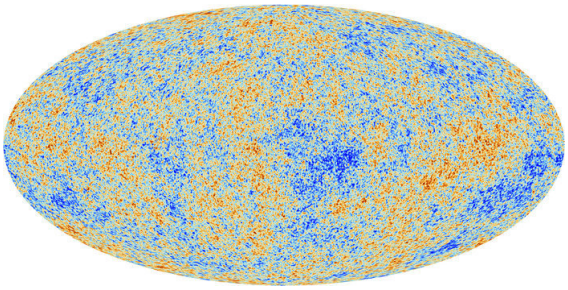

Figure 2.5: Anisotropy in cosmic microwave background as measured by Planck. The yellow and white (light) areas indicate a higher temperature and the blue (dark) areas indicate a lower temperature. CMB anisotropy is used to calculate a power spectrum for these fluctuations, which can then be analyzed to measure the fractions that make up the ΛCDM model. `http://www.esa.int/spaceinimages/Images/2013/03/Planck_CMB`

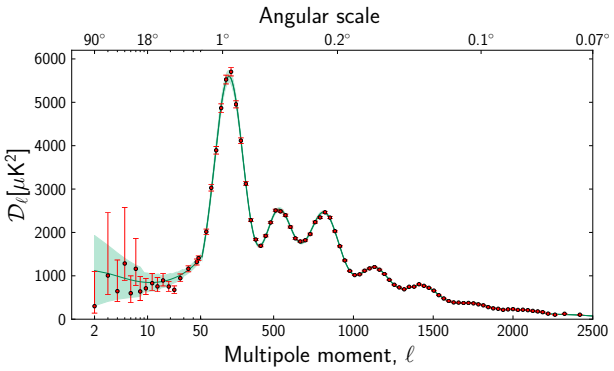


**Figure 37.** The 2013 *Planck* CMB temperature angular power spectrum. The error bars include cosmic variance, whose magnitude is indicated by the green shaded area around the best fit model. The low-$\ell$ values are plotted at 2, 3, 4, 5, 6, 7, 8, 9.5, 11.5, 13.5, 16, 19, 22.5, 27, 34.5, and 44.5.

Figure 2.6: How does Planck take observations of the cosmic microwave background and turn that data into information about the mass fractions of the universe? The process is complex, but an important step is creating the above plot. The multipole moment (on the x-axis) is related to the structure of the fluctuations in the CMB. The y-axis indicates the intensity of the fluctuations. The features of this power spectrum (i.e., the heights and positions of the peaks) represent proportions of dark matter, dark energy and baryonic matter. Analyzing fits of this plot allows measurement of the values reported in table 2.1.

fraction of the baryonic matter to be much too low for MaCHOs to account for a significant portion of the dark matter in the universe.

## Planck Power Spectrum

Planck measures mass fractions via observations of the Cosmic Microwave Background (CMB). These ancient photons permit gains of insight into the history and structure of the

universe. The fluctuations in the CMB have been meticulously mapped by Planck (and others); see figure 2.5 The temperature fluctuations are measured, and their amplitudes and structures are mapped to a power spectrum; see figure 2.6. The power spectrum is then fitted with lambda-CDM variables and others to calculate the outputs as in Table 2.1.

### 2.1.5 Cosmology: Early Universe

After the Big Bang, many phases follow (see Figure 2.7). Immediately after the Big Bang is known as the Planck epoch, which was quickly followed by the inflationary period. At this time the universe was composed of a quark-gluon plasma. Baryogenesis is the next phase, meaning the breaking of the matter/antimatter symmetry. Then baryons formed from the quarks. As the more massive particles cooled/slowed, radiation came to dominate the universe. Next is the period of nucleosynthesis, or (light) element formation. After this, matter dominated the universe. The CMB (cosmic microwave background) decoupled from matter. Then galaxies began to form. Today, the universe is dominated by dark energy.

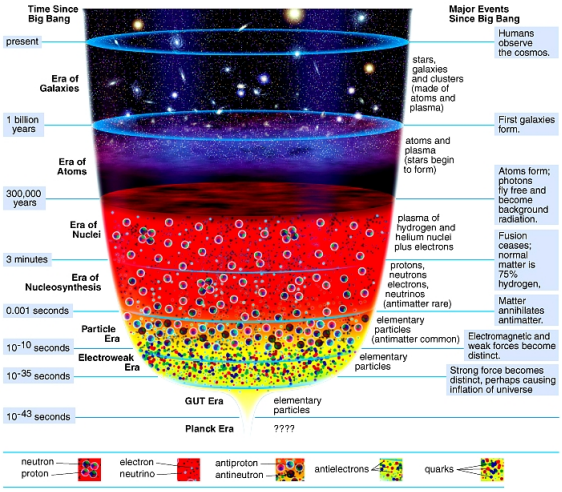


Figure 2.7: The phases of the Big Bang and evolution of the Universe. (Source: U. of Arizona Lectures: http://ircamera.as.arizona.edu/NatSci102/lectures/eraplanck.htm - originally from "The Essential Cosmic Perspective", by Bennett et al.)

### 2.1.6 Cosmology: Structure

Considerations of how structure in the Universe formed gives arguments for cold rather than hot dark matter. The moment when the exchange of momentum between WIMPs and radiation ceases to be effective is called kinetic decoupling. The time at which this decoupling occurs affects WIMP speeds. If kinetic decoupling happens during the reheating phase of LTR (low temperature reheating) models, WIMP speeds decrease. This could cause much smaller dark matter structures, mini-haloes in our galaxy, hotter WIMPs, warm instead of cold dark matter. Cold Dark Matter would decouple from the primordial plasma before baryons do, thus providing potential wells to trap the baryons in, so that the universe can form with the levels of structure that we observe [13]. If galaxies formed in an environment where the dark matter was warm, the structure would form "from the top down;" cold dark matter would allow a "bottom-up" type of structure formation. Observations of the structure of galaxies favor bottom-up formation, therefore cold dark matter is preferred.

### 2.1.7 Cosmology: Nucleosynthesis

Big Bang nucleosynthesis (BBN) occurs 200 seconds after the Big Bang, when T $\simeq$ 0.8 MeV. The trace we have for this period is the abundance of light elements such as D, $^4$He, and $^7$Li. BBN only lasts while the universe was hot enough for nucleosynthesis. The temperature of the universe is reliant on its expansion rate, which is in turn reliant on the baryon-to-photon ratio. Therefore, by measuring the relic abundances of light elements and the cosmic microwave background we can infer the baryon fraction or density of the universe. Since this turns out to be only about 4%, any other matter must be accounted for by non-baryonic particles. [14] WIMPs with mass $\gtrsim$ 100 MeV will freeze-out before BBN; therefore any such WIMPs that still exist today would have formed before the period of nucleosynthesis. WIMPs would thus be the earliest remnants and give (if discovered) the first pre-BBN information. Since they interact so seldom, it's reasonable to assume that if we find one, it was not only created before nucleosynthesis, but likely hasn't interacted since then either. The results from the Planck telescope observations and calculations working back from light

element abundance today via nucleosynthesis theory are in exceptional agreement. This is quite validating to the premise that dark matter exists, since these methods are independent.

## 2.2 Dark Matter Halo

The basic structure of the dark matter halo can be inferred from astronomical observations such as galaxy rotation curves, as well as simulations. We believe that the dark matter is located in a spherical, nonrotating halo, concentric with the galaxy it permeates and surrounds. Kinematic analyses indicate dark matter particles likely travel at velocities of approximately 200 km/s. The dark matter mass density throughout our galaxy is generally assumed to be approximately 0.3 $GeV/c^2$ per cubic centimeter. These results come from detailed models of the dark matter halo, as described in [15], for instance. These values are commonly assumed among dark matter experiments.

## 2.3 Dark Matter Candidates

Dark matter candidates need to fulfill many requirements. They must match relic density, be cold, neutral, be consistent with Big Bang nucleosynthesis (BBN), leave stellar evolution unchanged, be suitable for direct dark matter searches, be compatible with gamma ray constraints and astrophysical bounds, and (preferably) be experimentally discoverable.

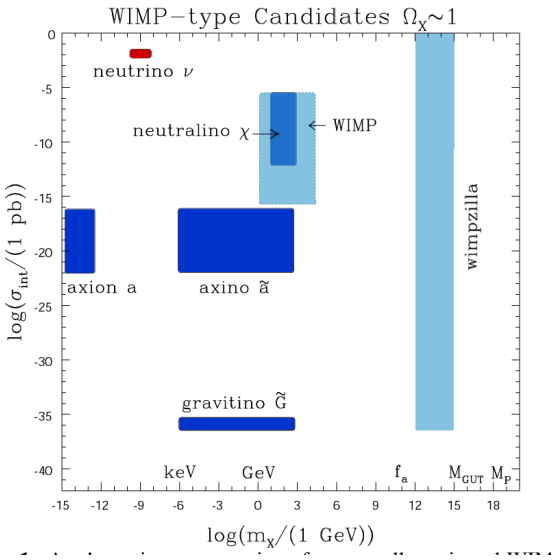


Figure 2.8: A number of dark matter candidates exist. WIMPs are considered by many to be the preferred candidate, due to their well-motivated theoretical background (see WIMP "miracle") and the good likelihood that, if real, they could be detectable. Other prominent candidates which are being investigated include axions and neutrinos, but all those listed in this figure are in theory possible dark matter candidates. Time will tell which one, few, or whether any of these are actually what dark matter consists of. [8]

#### 2.3.0.1 WIMPs

WIMPs (weakly interacting massive particles) are appealing for a number of reasons. WIMPs exist in well-motivated particle theories, such as Supersymmetry. WIMPs are naturally produced with the correct thermal relic density (this is the WIMP "miracle"). WIMPs predict signals that are experimentally testable now and soon.

**WIMPs in the early universe** In the early universe, when WIMPs were first formed annihilation took place as in the left side of figure 2.9, before the flat line starts to curve down, meaning that WIMPs frequently annihilated and were produced in turn. Some time later, the temperature dropped, so that WIMP production ceased, although annihilation continued

(this is the negative-slope, curved portion of the graph). "Freezeout" occurs when the WIMPs cease annihilating due to low cross section and low number density, leaving a steady relic density that we anticipate to be essentially unchanged from the original time of freezeout to present day. It is interesting to note that WIMPs with mass $\gtrsim 100$ MeV will freeze-out before BBN (Big Bang Nucleosynthesis). WIMPs would thus be the earliest remnants and give (if discovered) the first pre-BBN information. Since WIMPs interact so seldom, it's reasonable to assume that if we find one, it was not only created before nucleosynthesis, but likely hasn't interacted since then either. If dark matter really is WIMPs, then this will provide an intriguing window into the early universe.

**WIMP Freezeout** WIMP freezeout occurs when density and temperature drop low enough so that the annihilation rate is less than the Hubble expansion rate. Then WIMP number per comoving volume becomes (approximately) constant. Thus, number density decreases as volume increases. (Speaking in terms of comoving volumes is necessary, since the universe is continually expanding.) At freezeout temperature (when the WIMP annihilation rate $\sim$ O(Hubble expansion rate)), WIMP annihilation becomes negligible and the WIMP abundance per comoving volume becomes steady. Then:

$$T_{fo} \simeq \frac{m_\chi}{20}; v_{fo} = \left(\frac{3T_{fo}}{2m_\chi}\right)^{1/2} \simeq 0.27c \tag{2.2}$$

Smaller annihilation cross sections lead to larger relic densities, thus the saying: "the weakest wins". WIMPs with stronger interactions are in chemical equilibrium for longer, and decouple when the Universe is colder, so their density is suppressed more than the density of WIMPs with smaller interaction rates.

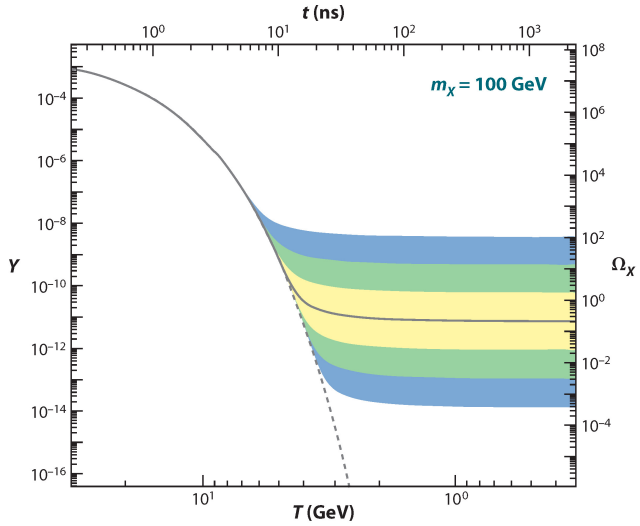


Figure 2.9: Early in the universe, WIMPs were produced and annihilated in similar numbers. As the temperature of the universe decreased, WIMP production was no longer possible. As the WIMPs annihilated and were not replaced, their number density decreased over time. At some point (known as "freezeout," the WIMPs became so spread out, that given their low interaction rate, annihilation rates dropped to approximately zero. This is why we anticipate a steady amount of WIMPs in the universe today. The point of freezeout depends on the interaction rate of the WIMPs. [9]

**WIMP relic density** What is meant by relic density? WIMPs in chemical equilibrium in the early Universe naturally have the right abundance (or density) to be CDM (cold dark matter). In addition, the interactions that give the right WIMP density make the detection of WIMPs possible. The current density of WIMPs (number density = n):

$$\frac{dn}{dt} = -3Hn - \langle\sigma_{ann}\nu\rangle(n^2 - n_{eq}^2) \tag{2.3}$$

where H is the Hubble parameter.

The law of entropy conservation is:

$$\frac{ds}{dt} = -3Hs \tag{2.4}$$

where s is entropy density. Also:

$$\frac{dY}{dx} = \frac{1}{3H}\frac{ds}{dx}\langle\sigma_{ann}\nu\rangle(Y^2 - Y_{eq}^2) \tag{2.5}$$

where Y = n/s, x = m/T, and T = photon temperature.
At high temperatures, Y (=n/s) closely tracks its equilibrium value. As time increases and temperature decreases, the Y equilibrium value falls off but Y freezes out and becomes constant. (see Figure 2.9)

Relic density is: $\Omega_\nu h^2$. Freezeout happens later (at smaller WIMP densities) if WIMP annihilation cross section is larger. The present WIMP relic density is:

$$\Omega \cdot h^2 \approx \frac{3 \times 10^{-27} cm^3/s}{\langle\sigma_{ann}\nu\rangle} \tag{2.6}$$

Weak cross sections give the right order of magnitude dark matter density. Weak cross sections give freezeout time

$$T_{fo} \simeq \frac{m}{20} \tag{2.7}$$

where m is the WIMP mass. Standard WIMP productions says that WIMPs were produced in collisions between particles of the thermal plasma during the radiation-dominated era. WIMP pairs are from/to particle/antiparticle pairs. The WIMP couples to neutrons or protons very similarly ($f_n \approx f_p$).

**Assumptions for WIMP "miracle"** The freezeout temperature depends on the mass of the WIMPs, the interactions of the WIMPs, and the Hubble parameter. The freezeout temperature plays a prominent role in determining WIMP relic density. In calculating the relic density of WIMPs, we assume some conditions for the pre-BBN Universe. We assume that entropy of matter and radiation was conserved, that WIMPs were produced thermally, that the WIMPs decoupled while the Universe's expansion was dominated by radiation, and that WIMPs were in kinetic and chemical equilibrium before decoupling.

**Calculating Backgrounds** When searching for WIMP dark matter, we can calculate the differential event rate. Usually reported in units of counts/kg/day/keV (this is the differential

rate unit: "dru"), this rate is as follows:

$$\frac{dR}{dE_R} = \frac{\rho_0}{m_N m_\chi} \int_{v_{min}}^{\infty} v f(v) \frac{\mathrm{d}\sigma_{WN}}{\mathrm{dE}_R}(v, E_R)\, \mathrm{d}v \tag{2.8}$$

Differential Event Rate. $\rho_0$ is the local WIMP density. $\frac{\mathrm{d}\sigma_{WN}}{\mathrm{dE}_R}(v, E_R)$ is the differential cross-section for WIMP-nucleus elastic scattering. f(v) is the WIMP speed distribution.

The WIMP-nucleon relative speed $\sim 100$ km/s. Elastic scattering of WIMPs and nucleons is extremely non-relativistic. (p.348) The recoil energy of a nucleon after a WIMP scatter is:

$$E_R = \frac{\mu_N^2 v^2 (1 - cos\theta^*)}{m_N} \tag{2.9}$$

where $\mu_N = \frac{m_\chi m_N}{m_\chi + m_N}$, the WIMP-nucleus reduced mass, and $\theta^*$ is the scattering angle in the center of mass frame. The minimum WIMP speed to cause a nuclear recoil energy of energy $E_R$ is:

$$v_{min} = \sqrt{\frac{m_N E_R}{2\mu_N^2}} \tag{2.10}$$

Event rate R (/kg/day):

$$R = \int_{E_T}^{\infty} dE_R \frac{\rho_0}{m_N m_\chi} \int_{v_{min}}^{\infty} v f(v) \frac{d\sigma_{WN}}{dE_R}(v, E_R) \mathrm{d}v \tag{2.11}$$

where $E_T$ is the threshold energy, the smallest detectable recoil energy for a detector.

The WIMP-nucleus differential cross section depends on particle physics inputs, WIMP interaction properties, WIMP-quark interaction strength, microscopic description of model, and effective Lagrangian for interactions of WIMPs with quarks and gluons. The WIMP-nucleus cross-section can be separated into spin-independent (scalar) and spin-dependent contributions.

The WIMP-nucleus cross section:

$$\frac{d\sigma_{WN}}{dE_R} = \frac{m_N}{2\mu_N^2 v^2} (\sigma_0^{SI} F_{SI}^2(E_R) + \sigma_0^{SD} F_{SD}^2(E_R)) \tag{2.12}$$

The form factor F depends on q, the momentum transfer ($q = \sqrt{2 m_N E_R}$). $\sigma_0$ is the cross section at zero momentum transfer. (p.349) The differential event rate is directly proportional to the local WIMP density, and uncertainties in local WIMP densities directly affect

WIMP differential event rates. The canonical local WIMP density is:

$$\rho_0 = 0.3 \text{ GeV/cm}^3 \tag{2.13}$$

This is the value traditionally used to calculate exclusion limits.

#### 2.3.0.2 non-WIMP candidates

Motivations for non-WIMP candidates include minimality, experimental anomalies, and to highlight our dark matter ignorance. Non-WIMP candidates share many desired properties with WIMPs, including superWIMP candidates that inherit correct relic density through decays, and WIMPless candidates that have no weak-scale mass, no weak interactions, but the correct thermal relic density. WIMPless dark matter provides new indirect target signals: WIMPless dark matter $\rightarrow$ neutrinos in the Sun (detectable by Super-K), and additional targets for photons, positrons, and other annihilation products.

**Axions and axinos** Axions are a proposed particle which was invented to solve a puzzle in particle physics. Experiments regarding CP violation in QCD gave very different results from those which were expected; introducing a new symmetry alleviates the problem. Breaking this symmetry produces a particle which has a very small mass and interacts very slightly with the strong and weak forces. This particle, the axion, is a boson, and can interact with photons. Experiments look for this process by creating strong magnetic fields in their detector. Axions have not been detected but could in theory be a dark matter candidate. Axions also have a proposed supersymmetric superpartner, the axino, which is also a possible dark matter candidate.

**Neutrinos** Neutrinos could possibly account for some of the observed dark matter, but various reasons preclude it from being "the" dark matter particle. First of all, neutrinos travel at such high speeds that they are relativistic and therefore classified as *hot* dark matter. Although we have not yet pinned down the masses of the three standard model neutrinos, the upper limits indicate that the neutrino mass is just too small to account for

all the dark matter in the Universe. The reason why you can't just have more neutrinos of a small mass has to do with the fact that neutrinos are fermions. Since fermions must abide by the Pauli exclusion rule and not share the same quantum state, it turns out that there is a finite number of neutrinos that can be packed into a given amount of space. Given the space available in galaxies and galaxy clusters relative to the mass of the neutrino and the expected mass of the dark matter, there just isn't enough space for neutrinos to account for the dark matter. We also know that mapping of the cosmic microwave background radiation points toward cold (nonrelativistic) dark matter rather than hot, as do simulations regarding the structure formation of the Universe. Neutrinos, then, at the least cannot be the primary dark matter particle.

## 2.4 Dark Matter Detection

### 2.4.1 Colliders

Dark matter could be created in a particle collider such as the LHC, but would not be directly detectable. Rather, it would be "seen" in terms of missing energy or missing momentum (as neutrinos are). Colliders have not found dark matter or SUSY, and have made exclusion regions. Colliders can see very low in energy (in comparison to direct/indirect experiments) due to their precise energy measurements of particles.

### 2.4.2 Indirect Detection

Indirect detection of dark matter involves measuring products which result from dark matter annihilations. When dark matter particles annihilate together, they can produce neutrinos, photon pairs, electron/positron pairs, and others. Excesses in some of these channels have been detected, pointing toward dark matter signals, although nothing conclusive has been confirmed as of yet.

While most annihilation of dark matter ended after freezeout due to low density of WIMPs, dark matter can be "caught" in large objects like the Sun or Earth, and a higher density builds up in these bodies, to the point where annihilation rates are significant. [11]

Satellite telescope experiments in space provide much of the most interesting indirect dark matter experimental results. (Taking the detector above the atmosphere is a requirement for many experiments, as once particles interact with the atmosphere, a whole new level of complexity enters the picture.) PAMELA and Fermi both see excesses in cosmic ray positrons which could be explained by dark matter, although the results cannot be considered definite proof of dark matter due to uncertainties in rate expectations due to pulsars, the complexity of the galactic center, and other factors.

Neutrino telescopes also contribute to the indirect dark matter search, as neutrinos from the Sun or the galactic center could come from dark matter annihilations. One prominent neutrino detector, IceCube, sees no sign of an excess in neutrinos consistent with a dark matter result; neither has any other neutrino detector reported signs of dark matter.

### 2.4.3 Direct Detection

Dark matter is directly detected when a WIMP scatters off a nucleus in a detector, whose recoil can be detected. There are particle physics uncertainties in the determination of scattering cross section, and astrophysical uncertainties in the local density and velocity of WIMPs. The WIMP direct detection rate depends on astrophysical input (local dark matter density, local dark matter velocity distribution) and particle physics input (nuclear form factors, interaction cross sections, and theoretical framework). Events which scatter off electrons are not likely to be WIMPs and are considered background.

Since direct detection is based on measuring collisions between WIMPs and nuclei, a method for detecting these collisions is needed. In fact there are three primary methods of detecting this sort of collision: Scintillation, Ionization, and Phonons. These methods are discussed in Chapter 3.

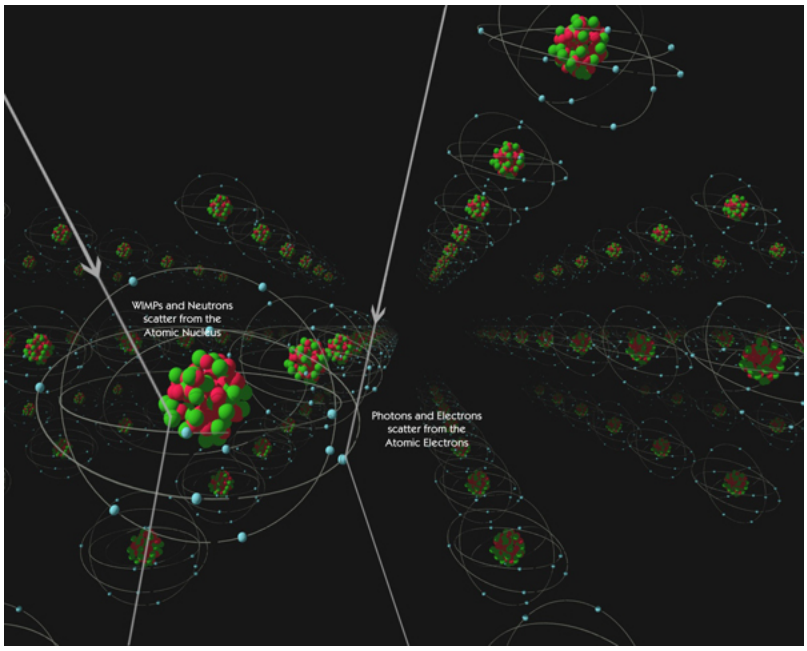


Figure 2.10: A particle scatters off a nucleus or an electron. WIMPs are expected to interact only with the nucleus, so electron recoil events are significant backgrounds. Distinguishing between nuclear and electron recoils is a very useful feature of a dark matter detector. `http://cdms.berkeley.edu/Education/DMpages/essays/science/directDetection.shtml`

# Chapter 3

# Direct Detection: State of the Field

This chapter is intended to give brief summaries of most of the relevant direct detection experiments that are operating or about to be operating as of summer 2014, as well as an overview of their detection methods. The chapter opens with discussion of channels used for direct detection accompanied by brief descriptions of experiments. The most important experiments will then be discussed in further detail, including consideration of possible signals and the effect of certain important exclusion results.

## 3.1 Detector Channels

There are three types of signals which can be observed in direct detectors. They are all results of WIMP-nucleus recoil and are proportional to the recoil kinetic energy. Some experiments detect two types of signals, which is especially useful for distinguishing between electron recoil and nucleus recoil events. Quenching behaves differently.

### 3.1.1 Scintillation

Scintillation occurs when photons created as the recoiling particle collides with other particles escape the crystal and can be detected. Collisions with detector material excites the nuclei, which then emit photons as they return to their ground state. These photons then can be detected with a photomultiplier tube (PMT). In direct detection dark matter experiments, most scintillation detectors use liquid noble gas or inorganic crystals as their target material. Pulse-shape discrimination can give useful information about the event as

well as simply the amount of light. In some cases, pulse-shape analysis can discriminate between electron recoil and nuclear recoil events, which is extremely useful for dark matter detection since electron recoil events are a very high background. A brief overview of selected direct detection experiments which use scintillation follows.

## NaIAD, DAMA, DM-Ice, ANAIS

These experiments use NaI(Tl) as their target. These experiments read out scintillation signal only. NaI(Tl) crystals have been used for particle detection experiments since 1948, and was the material used in the first widely used scintillation detectors. Hofstadter developed the thallium-infused NaI detector material around this time. NaI needs to be shielded from water, so is usually encased in a thin copper casing, or otherwise shielded from the atmosphere. Crystals will absorb water and lose their usefulness if exposed to even small amounts. NaI crystals must also be protected from rapid changes in temperature and mechanical shock in order to preserve their function. NaI(Tl) has a light yield of 38,000 photons/MeV. Some other properties of NaI(Tl) include a density of 3.67 g/cm$^3$, a wavelength of maximum emission of 415 nm, an index of refraction of 1.85, a decay time of 230 ns, and an alpha-to-beta ratio (or quenching factor; see chapter 6) of about 0.66 or 0.67 [16].

NaIAD (NaI Advanced Detector) is an early example of a sodium iodide dark matter detector. Gathering data from 2000-2003, NaIAD placed limits on the WIMP phase space, but these limits were not sufficient to speak to the DAMA claim (made in 2000 and often since that time). 10.6 kg-years of data was gathered. Interestingly, NaIAD notes that DAMA originally began with a similar analysis to that of NaIAD (pulse shape analysis), with null results, but then switched to an annual modulation analysis method, which yielded their discovery claim. [17]

DAMA (DArk MAtter)

## KIMS

KIMS stands for Korea Invisible Mass Search. This experiment, located at Seoul National University, uses CsI(Tl), scintillation only. CsI(Tl) has a light yield of 65,000 photons/MeV [16], and is more durable in terms of mechanical shock and hygroscopic sensitivity than NaI(Tl). KIMS is a $\sim$ 100 kg detector composed of twelve crystals, and reports on data taken over a full year (nearly 25,000 kg-days of data). The crystals are arranged in a 3x4 array, and signal is read out via PMT. The search uses pulse shape discrimination to search for individual dark matter events. No dark matter signature is found, and much of the DAMA region is excluded (see section 3.2.1 for discussion on DAMA result and discovery claim). [18] KIMS has also reported on an analysis they have done on annual modulation, for further comparison to the DAMA result. This analysis considers 2.5 years of detector operation, amounting to more than 75 ton-days of data. The modulation is reported to be consistent with null [19].

## MiniCLEAN, DEAP-3600

MiniCLEAN and DEAP-3600 search for dark matter via scintillating liquid Ar. LAr is less expensive than liquid Xe, another liquid scintillating noble gas often used for dark matter searches. MiniCLEAN consists of a tank of 500 kg of liquid Ar, surrounded by photomultiplier tubes which detect the scintillation light; it can also run with liquid neon. DEAP-3600 runs with liquid Ar only, but can accommodate 3600 kg. Both detectors purify their liquid targets throughout operation. MiniCLEAN and DEAP-3600 are in many ways very similar (including location; both run at the SNOLAB underground laboratory), but have several key differences. One is the temperature at which their PMTs run; DEAP has "warm" PMTs, while MiniCLEAN's PMTs operate at a cooled temperature, inside the cryogen which holds the liquid scintillator. [20] Of particular interest with regard to MiniCLEAN; the opportunity to run with two different target materials in the same detector may allow special insight into differences both in background as well as potential dark matter signals when the target nuclei have different atomic numbers. MiniCLEAN is on track to

begin taking data sometime in 2014 [21]. DEAP-3600 is on a similar schedule, looking to commission their detector in summer 2014 and begin data taking in the fall [22].

### 3.1.2 Phonons (heat, vibration)

Phonon excitations occur when the recoil kinetic energy excites the crystal. Thermal sensors then detect the change in temperature of the crystal. These experiments are usually cryogenic in order to increase the sensitivity to small changes in temperature. A brief overview of selected direct detection experiments which use phonons follows.

#### CRESST

CRESST (Cryogenic Rare Event Search with Superconducting Thermometers) is a low-temperature (10 mK) experiment which uses phonon detection as its primary method of measuring deposited energy. Its target is a scintillator, $CaWO_4$. The phonon signal is read out using TES (transition edge sensors). The change of temperature in the calorimeter is then analyzed to determine the energy deposited. [23]

#### CUORE

CUORE (Cryogenic Underground Observatory for Rare Events) is a tellurium dioxide ($TeO_2$) bolometry experiment designed to search for neutrinoless double beta decay. Its low threshold, however, allows it to also carry out a direct dark matter detection search. CUORE is located in the Gran Sasso Underground Laboratory in Italy. Its $TeO_2$ crystals are instrumented with Ge thermistors to measure temperature changes from the standard detector temperature of 10 mK. CUORE cannot distinguish between electron and nuclear recoils, but will search for dark matter via the annual modulation properties of the expected WIMP signal. CUORE-0, with 52 bolometers of 750 g $TeO_2$ each, and CUORE (98 bolometers) anticipate being able to report limits or signs of discovery with only a few years of operation. [24]

### 3.1.3 Ionization

The ionization signal is created as the recoiling particle collides with ions and electrons, creating ionized electrons which can be collected by means of an electric field.

## CoGeNT

CoGeNT (Coherent Germanium Neutrino Technology) is a PPC (p-type point contact) Germanium detector deployed in 2009 at the Soudan Underground Laboratory in Minnesota. The detector mass is 443 g. PPC detectors allow a very low energy threshold, which is of course quite useful in a dark matter search, since an exponential rise at low recoil energies is expected. The CoGeNT prototype, a small detector in a shallow underground location, was able to exclude in 2008 [25] the last unexplored area of the DAMA preferred region. With only one channel in use, CoGeNT focuses on an annual modulation search. CoGeNT has seen a modest modulation, which has persisted over several years. The reported statistical significance of the modulation has actually reduced somewhat as CoGeNT gathers more data: in 2011 [26] , they report 2.8 sigma with 442 live days of data-taking, while in 2014 the corresponding number is 2.2 sigma, with 1129 live days. [27] This annual modulation is accompanied by an unexplained excess of events in the energy region where the modulation is observed. While the statistical significance does not amount to a discovery (nor do they claim it to), the phase is consistent with what we expect for WIMPs (and with the modulation seen by DAMA). CoGeNT data is publicly available.

### 3.1.4 Multiple Channels

Many recent direct detection experiments instrument their target material with two types of readout capabilities. Comparing these two signals (scintillation and ionization, ionization and phonons, etc) allows in many cases a determination to be made whether the recoil was due to a nuclear collision or a collision with an electron. This eliminates most forms of backgrounds, and allows a particular event to be labeled background or consistent with the expectations for a WIMP.

**Scintillation+Ionization: XENON, LUX** These experiments use liquid Xe as their target. They use scintillation and ionization as their dual signal. Liquid Xe is expensive, and a significant amount is required in order to have enough fiducial volume.

**Scintillation+Phonons: CRESST-II** CRESST-II is the upgrade of CRESST, and adds another channel: scintillation. This is particularly useful for discrimination between nuclear and electron recoil.

**Ionization+Phonons: CDMS, EDELWEISS** CDMS is a cryogenic experiment which reads out phonons and ionization signal. EDELWEISS uses phonons and ionization as well.

### 3.1.5 Bubble Chamber: COUPP

Chicagoland Observatory for Underground Particle Physics (COUPP) is a bubble chamber dark matter experiment. Searching for dark matter via bubble chamber is a threshold-based process, in that either nucleation occurs (i.e., a bubble is formed) or it does not. No energy measurement is made; the bubble is formed if the interaction gives off energy above a particular threshold. The COUPP chamber is filled with $CF_3I$.

### 3.1.6 Annual Modulation

Dark matter interactions are expected to modulate annually due to the orbit of the earth around the sun and the sun's path through the galaxy as it rotates. The speed of the Sun through the galaxy is 220 km/s, so this is the effective velocity of the dark matter if we consider the Sun to be unmoving. The dark matter halo does not rotate. We then have an effective "dark matter wind" from the perspective of a stationary sun. When the earth's path travels with the wind, we have a dark matter interaction minimum, but when the earth's path travels against the wind, we have a dark matter interaction maximum.

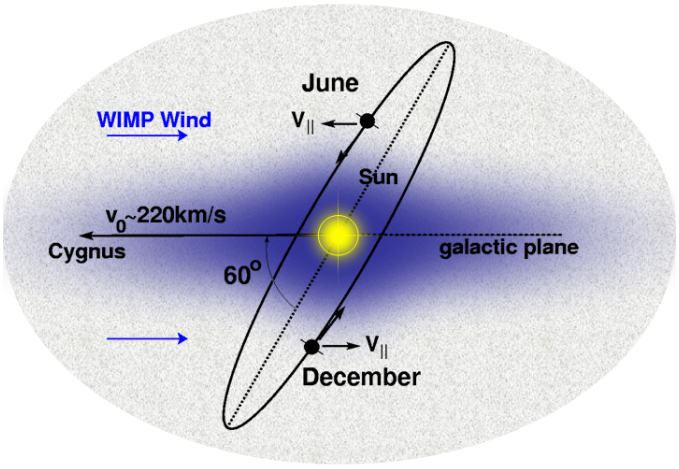


Figure 3.1: The WIMP dark matter peaks at June 2nd, and is at a minimum six months later. This is due to the rotation of the Earth about the Sun and the motion of the Sun itself; the dark matter is itself nonrotating. Although the dark matter does not rotate, the effect to us on Earth is often compared to a wind; hence you will find references to the "WIMP wind".

## 3.2 Dark matter exclusion results vs. possible dark matter signals

### 3.2.1 DAMA

DAMA finds an annual modulation with a significance of $9\sigma$ in the range of a few eV [28] [29]. Their dark matter claim is complicated by the null results of CDMS(Ge), XENON100, and LUX, which all exclude the DAMA region. DAMA's extremely radiopure crystals, large mass and long run time make testing their claim a tall order.

### XENON

The XENON collaboration began with XENON-10 (10-kg of liquid xenon), and then progressed to XENON-100 (operating today). XENON-1T (one ton) is funded and will operate in the future. XENON uses the ionization and scintillation channels. Their threshold

is quite low, and their result one of the most severe limits. There is some question as to their understanding of the behavior of liquid xenon at very low energies.

## LUX

LUX is to first order quite similar to XENON. The basic search method is the same, and their null results agree, although LUX's limit is even more restricting than that of XENON-100.

## CDMS

CDMS (Cryogenic Dark Matter Search) uses phonon and ionization detection to search for dark matter. CDMS operates Ge and Si ZIP (Z-sensitive ionization and phonon) detectors at a temperature of 40 mK. They have not seen dark matter in their Ge detectors (aside from two inconclusive events in the signal region) and have published an exclusion limit [ref]. Their analysis hinges on calculating the "ionization yield," which is the ratio of ionization signal to phonon signal. Electron recoil events have a high ionization yield, while nuclear recoil events have a low ionization yield. This allows for discrimination between background and signal. The primary background is due to surface effects. Surface (electron recoil) events have an artificially low ionization yield, due to reduced ionization signal. CDMS has not found annual modulation. The CDMS experiment is composed of two types of detectors, Ge and Si. The Si detectors have detected 2 unexplained WIMP-like events [10] The data set used for this analysis was gathered by 8 of the 11 CDMS Si ZIP detectors (each detector is 106 grams), over a 15-month period. There is a 5.4% chance that the backgrounds expected could be responsible for these events. The CDMS collaboration considers these events to be more likely to be explained by WIMPs than by known backgrounds, but refrains from making a discovery claim. The CDMS Ge detectors do not detect any excess; all events are consistent with known backgrounds. This possible disparity could be most informative; why might the Si detectors register WIMPs while the Ge detectors in the same apparatus does not? This could be due to differences in the two elements: Si has an atomic mass of 28

g/mol, while the atomic mass of Ge is 72.6 g/mol. The lighter Si nuclei are more likely to interact with a lower-mass WIMP ($\sim$10 GeV/c$^2$) in terms of scattering kinematics. [10]

### CRESST-II

CRESST-II, the successor of CRESST, is a cryogenic dark matter detector which has measured a signal unaccounted for by background, which may be explained as a WIMP signal. CRESST-II has gathered 730 kg-days of data between 2009 and 2011. Sixty-seven events have been found in the phase space in which WIMPs would be expected, which were originally found at a 4-sigma level to be insufficiently explained by known backgrounds. [23] However, further data-taking and detector upgrades has not confirmed the potential signal, and the newest results instead report exclusion limits. [30]

## 3.2.2 Summary of possible signals

**DAMA** The DAMA experiment sees a definite modulation which is roughly in phase with the expected behavior of dark matter WIMPs.

**CoGeNT** CoGeNT finds some dark matter candidate events, and sees a possible annual modulation.

**CDMS-Si** See figure 3.2. The Si detectors of CDMS have detected two events which cannot be explained by known backgrounds. [10]

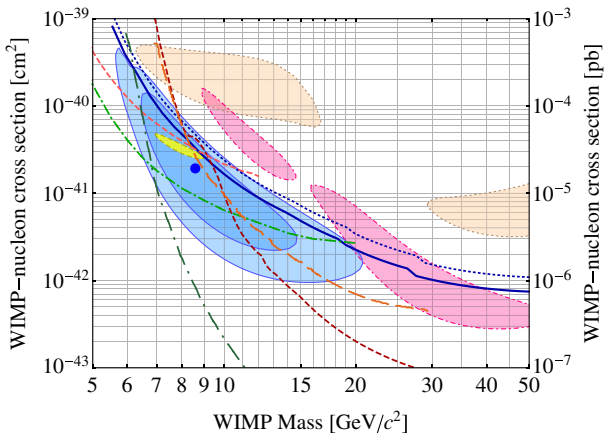


Figure 3.2: CDMS Si and Ge results and others. CDMS-Si results are represented by the blue dotted and solid lines/regions. CDMS-Ge results are in dark and light dashed red. EDELWEISS is long-dashed orange, XENON10 (S2 only) is dash-dotted green, and XENON100 is long-dash-dotted green. CoGeNT preferred region is in yellow, DAMA/LIBRA region is in tan, and CRESST (signal no longer relevant) is in pink. Thus, we see that the tension in the field persists, and agreement between experiments which see signals is low." [10]

### 3.2.3 Summary of Current Limits

**XENON-100** XENON sees no WIMP events, and excludes the phase space favored by CDMS-Si, DAMA, and CoGeNT.

**LUX** LUX reports an exclusion limit which is even stronger than that of XENON-100.

**CRESST** CRESST-II does not see dark matter.

**CDMS-Ge** The Ge detectors of CDMS see no WIMP events, and excludes the CDMS-Si result as well as the potential signals found by DAMA and CoGeNT.

## 3.3 DAMA's annual modulation signal

Does DAMA really see dark matter? This is up for dispute despite their consistent and unquestioning claim in the affirmative. Determining the validity of their claim has been made more difficult as DAMA prefers to release only limited portions of their data to the scientific community for consideration.

### 3.3.1 DAMA: Discrepancy, potential explanations

DAMA's preferred region is excluded by CDMS-Ge, XENON, LUX, others...what does this mean? The community largely is skeptical of DAMA's results, but a reasonable alternate explanation of their results which has been difficult to come by.

DAMA's result clearly shows an annual modulation. If it were dark matter, we would expect confirming results from other direct detection experiments. Since this is not the case, the question arises: could DAMA be seeing the modulation of some known particle? One possibility stems from cosmic ray muons. These high-energy particles are reduced in quantity at the depths of DAMA and other dark matter experiments, but they are not entirely blocked. The flux of muons reaching the surface of the earth (or below it) correlates with the temperature of the atmosphere. This leads to a seasonal modulation, which is peaked in the warm summer months and at a minimum in the winter. In the Northern Hemisphere, this phase agrees, broadly speaking, with the phase expected for dark matter. So is DAMA seeing muons? In fact no: DAMA shields against muons, and implements a muon veto. However, the muons may not be entirely blameless. Muons have been known to interact with rock, knocking out neutrons. These neutrons are difficult to shield entirely, and would mimic a WIMP interaction quite well. So then is DAMA seeing muon-induced neutrons? It turns out that while the phases of muons and WIMPs are similar, they are not exactly aligned. Muons or particles produced by modulating muons are unlikely to explain DAMA's signal. For more discussion on this, please see these references: [31], [32], [33], [34]. For one interesting new proposal for an explanation for DAMA's observed modulation, please see [35].

## 3.4 Tension in the field, but also promise

While a great deal remains unknown, it does appear that we are on the cusp of understanding many things that are as of yet just outside our grasp. This is an intriguing time to be working in the dark matter field. In many ways, the most important issue in the field of direct detection is the conflict between the results of DAMA/LIBRA and the other experiments (LUX, CDMS-Ge, etc.). Resolving this confusion is a crucial step in moving our understanding of what dark matter either is or is not. The DM-Ice experiment is intended to produce results which will allow for this resolution.

# Chapter 4

# DM-Ice Detector

DM-Ice is a dark matter direct detection search for the annual modulation of dark matter. The prototype, DM-Ice17 (17 kg of NaI crystals) was deployed at the South Pole in December 2010. The primary purpose of the prototype was to demonstrate the feasibility of operating a dark matter detector deep under the ice, under irretrievable circumstances, rather than in a mine or underground laboratory, as is traditional. The full-scale DM-Ice detector, the components of which are beginning to be gathered together for assembly, will consist of order 250 kg NaI crystals, in order to give a decisive test of the DAMA/LIBRA result.

## 4.1 Motivation

The conflict between the DAMA dark matter discovery claim [28] and exclusion results from other detectors needs further results to resolve the matter. DM-Ice is a DAMA-like detector which can confirm or refute the DAMA results.

## 4.2 Special characteristics of DM-Ice

DM-Ice has several special characteristics to help with such a demanding and essential task as checking the DAMA claim. These include operating in the Southern Hemisphere, deployment in radioactively clean ice, and proximity to the IceCube Neutrino Observatory.

### 4.2.1 Southern hemisphere

The DM-Ice experiment will run in the southern hemisphere. The muon background (which is a possible explanation or component of an explanation for the observed DAMA modulation) is dependent on seasonal temperature variations in the atmosphere. This background is still present in the southern hemisphere, but is reversed in phase as the seasons are also. This phase reversal will allow for good resolution of the matter when results from DM-Ice are compared with DAMA data. Muon seasonal fluctuation has been measured by IceCube [36] (similar measurements at Gran Sasso also exist [37]).

### 4.2.2 Antarctic ice: a clean environment

DM-Ice will be located deep underground as DAMA is, but in an extremely radiopure environment. DAMA runs in the Gran Sasso underground laboratory in Italy, and has extensive shielding to reduce radioactive contamination from the rock (radon, etc) which surrounds the mine. DM-Ice will be surrounded by Antarctic ice, which has negligible background (see table 4.1). These estimates of isotope contamination in the glacial ice are derived from measurements of dust in the ice from core samples taken from glacial ice near Vostok [38] [39]. This dust is then assumed to have typical contamination as that of standard soil/rock. Contamination in the ice itself can then be inferred. Since the ice background is so low ($\geq 10^6$) less than in any underground rock environment), we may forgo extensive shielding of the detector: the predominant background will be from the crystal itself. DM-Ice may also be run in a traditional underground (in rock) setting before being deployed at the South Pole.

### 4.2.3 IceCube

DM-Ice will be installed below the IceCube detector, the largest neutrino telescope in the world. IceCube is located in a cubic kilometer of ice located beneath the surface of the South Pole which has been instrumented with more than five thousand DOMs (Digital

Optical Modules) containing PMTs to detect Cherenkov light from neutrino events as they interact in the ice.

IceCube can also function as a useful muon check for DM-Ice as it detects neutrinos for its own purposes, giving DM-Ice an external means of both determining muon rates near our detector and specifically identifying background events. Muon events in DM-Ice17 can be distinguished from gamma and alpha events by examination of pulse height (energy deposition) and pulse shape. Muon events have higher energy than gamma events, and can be distinguished from alpha events by the longer pulse shape of the muon events. Cross checking what we believe to be muon events with IceCube detection results confirms our ability to identify muon events in DM-Ice17. Another essential benefit for DM-Ice from the IceCube project is of course the existence of the technology and equipment which makes deep ice deployment possible. The Enhanced Hot Water Drill that can, in a matter of a few days, drill a hole a mile deep in the ice, is a key component of how this project is feasible.

## 4.3 DM-Ice17 Prototype

DM-Ice17, a prototype detector, was deployed in December 2010. This 17-kg NaI detector is composed of two detectors, each with one crystal (8.5 kg) and two PMTs. The PMTs output a signal which is processed, routed through the DAQ and sent north via satellite for analysis. It is necessary to protect the detector with a sturdy stainless steel pressure vessel in order to withstand the significant pressures which occur when the detector is frozen in upon deployment.

The two detector units have been deployed by attaching them to the bottom of two IceCube strings 7 and 79; see Figure 4.1 , which were themselves deployed toward the end of IceCube construction. Assembled using IceCube electronics and crystals from the NAIAD experiment, this prototype has proved the feasibility of running a dark matter detector at the South Pole deep in the Antarctic ice. The prototype has steadily sent data up north via satellite, and we have been optimizing and analyzing and using this information to inform

the planning of the full-scale DM-Ice detector. A report on the first data from this detector will be published in fall 2014; a draft may be viewed on the ArXiv at [40]

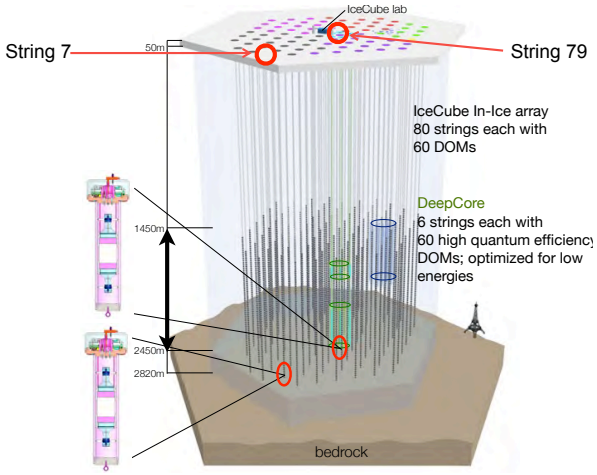


Figure 4.1: The DM-Ice17 detectors were deployed on the bottom of two IceCube strings: one near the center of IceCube, and one near the edge, as indicated.

### 4.3.1 DM-Ice17 construction

The NaI(Tl) crystals used in DM-Ice17 are inherited from NAIAD [17]. The entire crystal setup was effectively taken out of storage, sent to the Physical Science Laboratory in Stoughton , and used as the heart of the prototype detectors. Each of the two units consists of a NaI crystal (encapsulated in copper), two quartz light guides, two PMTs. Each of the two crystals weighs about 8.5 kg, and is equipped with its own light guides and PMTs. The crystals are encased in a thin layer of copper in order to protect the NaI from water and atmosphere on the curved edges, and have a thin quartz window protecting each flat end. These crystals were created to be very pure NaI(Tl), so as to provide a good target for the NAIAD dark matter search. Since the production of the DM-Ice17 crystals , crystal growing

techniques have improved, such that modern NaI(Tl) crystals can be produced at greater purity.

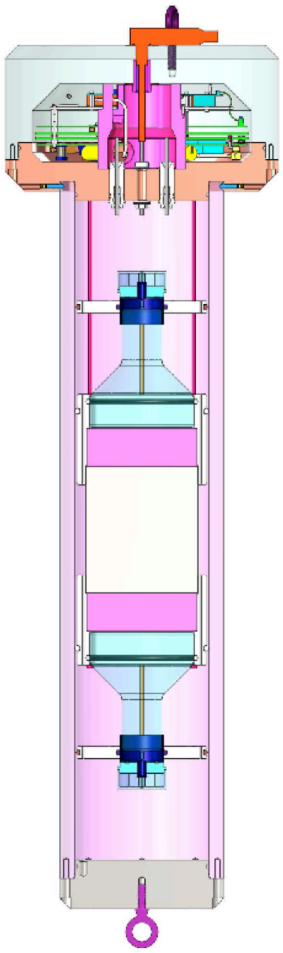

Figure 4.2: Engineering sketch of one of the prototypes. The NaI crystal (8.5 kg) is shown in white, the quartz light guides in pink, and the PMTs are in teal. Teflon rings are visible in white, stabilizing the intersections between crystal, light guides, and PMTs. For a detailed description and picture of the current geometry for DM-Ice17, please see figure 5.1.

Figure 4.3: NAIAD crystal just arrived at PSL from Boulby

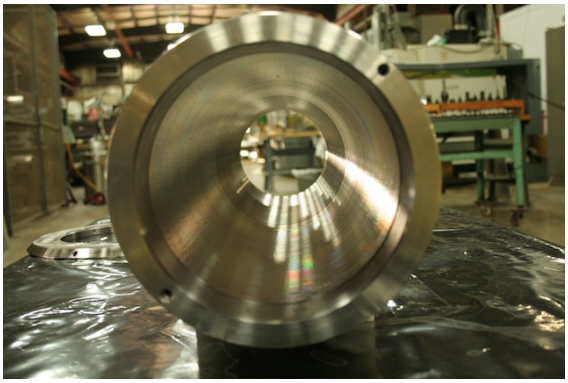

Figure 4.4: Stainless Steel Pressure Vessel. A pressure vessel is needed to protect DM-Ice17 from the high pressures during refreezing in the ice after deployment.

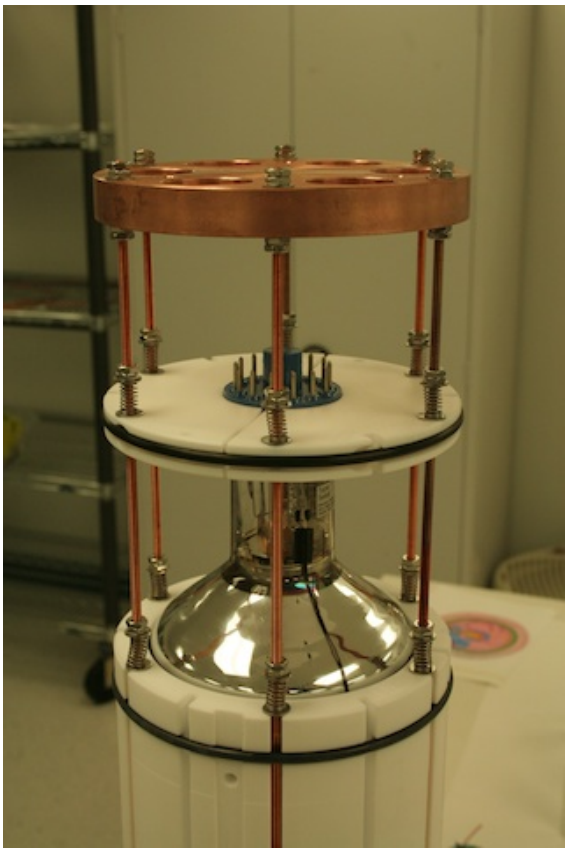

Figure 4.5: Prototype top, showing one of the PMTs, copper rods, and stabilizing teflon beneath the PMT

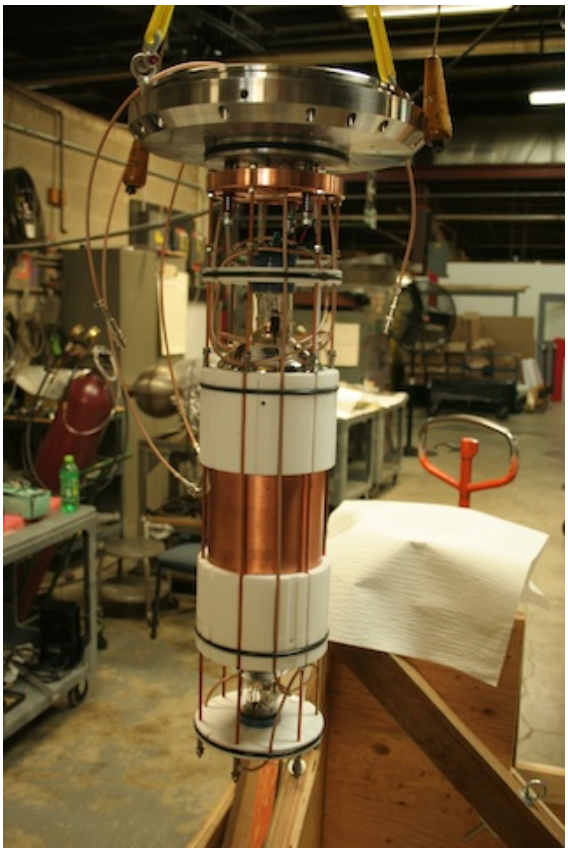

Figure 4.6: Prototype without pressure vessel

Figure 4.7: Prototype being placed into pressure vessel at Physical Sciences Laboratory

Figure 4.8: Prototype complete with pressure vessel and top hanging at Physical Sciences Lab before being packed for shipment to the South Pole in November 2010.

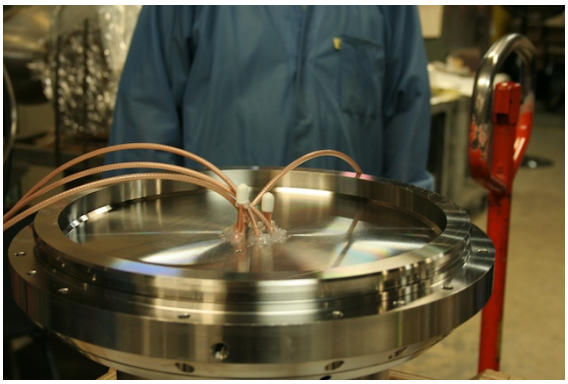

Figure 4.9: View of the top of the prototype detector before attaching the top of the pressure vessel

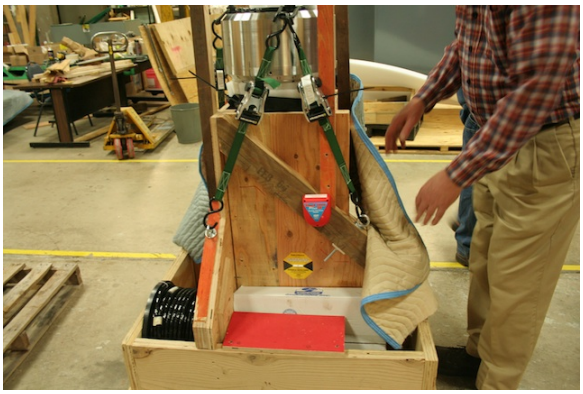

Figure 4.10: Packaging for shipping

Figure 4.11: Packaging for shipping

Figure 4.12: Packaging for shipping

Figure 4.13: Prototype sendoff

Figure 4.14: Prototype on plane

Figure 4.15: Prototype going down hole

### 4.3.2 Radio-Purity of DM-Ice Components

In preparation for data analysis, at the time of detector construction, certain pieces of material used in the detector were set aside for measurement purposes. Scraps from the stainless steel used to fashion the pressure vessel, for instance, as well as copper from the supporting copper rods were sent along with samples of drill ice water (the water melted during hot water drilling of the hole in which the detector was deployed) to SNOLAB to be counted.

The SNOLAB Low Background Gamma Facility is located deep underground (4600 feet) in Sudbury, Ontario, Canada. The DM-Ice17 samples were counted here, and measurements can be found in table 4.1. The SNOLAB counting facility operates by utilizing HPGe detector(s) which count gammas.

Table 4.1: Contamination levels of DM-Ice17 detector components in mBq/kg. Quartz measurements are from ILIAS database for 'Spectrosil B silica rod' [2], and PMT levels are from the low-background ETL 9390B datasheet (with increased $U^{238}$). Components that were measured specifically for this experiment at SNOLAB [3] are indicated by *. Components not shown in gamma/beta sim/data comparison are indicated by †.

| Material | $^{40}$K | $^{232}$Th | $^{238}$U ($^{234}$Th) | $^{238}$U ($^{226}$Ra) | $^{235}$U | $^{60}$Co |
|---|---|---|---|---|---|---|
| Quartz Light Guides | 0.50 ± 0.03 | < 4.9 | 12 | | – | – |
| ETL 9390B PMT | 9300 | 1000 | 2400 | | – | – |
| Steel Pressure Vessel * | 13.77 ± 6.38 | 6.49 ± 0.96 | 118.31 ± 60.11 | 2.28 ± 0.72 | 8.79 ± 1.68 | 7.19± 0.82 |
| Drill Ice * | 3.71± 1.36 | 0.55 ± 0.17 | 6.69 ± 3.02 | 0.39 ± 0.14 | 0.38 ± 0.21 | 0.12± 0.05 |
| Silicone Optical Gel * † | 39.50 ± 18.60 | < 0.12 | 2.08± 1.10 | 38.50 ± 61.00 | 0.96± 1.30 | 0.32± 0.42 |
| PTFE Supports * † | 0.34± 5.09 | 0.52± 0.44 | < 0.41 | 24.46 ± 21.37 | 1.92± 0.72 | < 0.089 |
| Copper Plate * † | < 5.13 | < 1.22 | 0.17 ± 0.92 | < 0.67 | 3.56± 1.79 | < 0.12 |
| Glacial Ice † | $\approx 3 \times 10^{-3}$ | $\approx 4 \times 10^{-3}$ | $\approx 10^{-3}$ | | – | – |

## 4.4 DM-Ice status: R&D for full scale detector

The full scale DM-Ice detector will be on the order of 250 kg of NaI(Tl). We anticipate using an array of smaller crystals in order to benefit from coincidence studies. See figure **??** for one idea of how the full scale detector may look; two detectors of 125 total kg each is the plan. A crucial aspect of assembling the full-scale DM-Ice detector is to obtain crystals of sufficient purity. As we consider different designs for the detector, we must determine what radioactive contamination is acceptable for all components of the detector.

# Chapter 5

# DM-Ice Background Simulation

## 5.1 Geant4 Background Simulation: Purpose and Goals

In order to understand the data received from DM-Ice17, it is necessary to understand our background. Since we are using an annual modulation search method, and not a zero-background method, we do not need to classify events as signal or background; still, in order to conclude whether or not a modulation is present, we must have a clear and detailed understanding of where our backgrounds come from. We should know the levels of radioactive contaminants in all parts of the detector and its surroundings.

Some of our materials were measured (see section 4.3.2 and table 4.1 ) at SNOLAB's Low Background Gamma Facility [41]. Other components of the detector were not able to be measured. These must be evaluated via simulation. Beyond understanding and interpreting the operation and data of DM-Ice17, simulation of these backgrounds from each component is essential in order to create the best possible design for the full-scale DM-Ice detector. We need to know what levels of cleanliness in each component will be acceptable in order to allow us to achieve our dark matter measurement goals. Further, the radioactive contributions from a particular component will impact choices of material and more. For instance, if the radioactive background from the stainless steel used for the pressure vessel is too large, then we may need to choose another material for the full-scale detector; for instance, titanium. Titanium is of course very expensive, so we prefer to use the steel if possible. Simulation provides essential information needed for decisions regarding materials selection for the full-scale detector.

Simulation also guides design of the light detection of the detector. DM-Ice17 has two quartz light guides between the crystal and its two PMTs, one guide and one PMT on each end of the crystal [see image]. This is done so that the radioactivity of the PMTs (primarily the glass in the windows) is a bit removed by distance from the crystal, to minimize the effect of the PMTs' impurities. Questions that need to be answered by simulation include, are the quartz light guides clean enough to do their job? Do we need more or less quartz to block the radiation from the PMTs? What degree of cleanliness in the PMTs would be needed in order to justify removing the light guides entirely? If we increase the purity of our crystal, how clean do the PMTs or PMT/light guide combos need to be in order to remain secondary backgrounds to the internal background of the crystal? Then, in terms of external background, how much contribution will the drill ice and Antarctic ice surrounding the detector contribute to the background as a whole? Is there a need to shield the detector from the ice itself, as is done in mine deployments? Simulating all these backgrounds thoroughly allows for decisions to be made on all these topics.

In order to answer all these questions, the Geant4 simulation package is used. GEANT means "GEometry ANd Tracking." This is a toolkit. ROOT then processes output simulation data (facilitates plotting). Geant4 is a descendant of GEANT3, which was originally developed for use by the collider experiments at CERN in Geneva, Switzerland. GEANT3 is FORTRAN based, while Geant4 is written in C++. GEANT3 was in use primarily from 1974 to 2000. Geant4 is today used primarily in particle physics, medical physics, space science, and other scientific areas.

### 5.1.1 Geometry

One way to describe a simulation such as that used for DM-Ice is that it consists of two basic parts: a virtual geometry, and instructions for what to do with this geometry. I inherited a rough version of the DM-Ice simulation from Matt Robinson of NAIAD; this was a working simulation with a preliminary geometry of the DM-Ice17 prototype. This simulation was used to create plots of anticipated backgrounds for the prototype, DM-Ice17.

This information indicated that the background from the ice would be negligible, and that the background from the crystal was likely to dominate. These were important pieces of information, which encouraged the group to go ahead with building and deploying the prototype in the first place. However, once the prototype was built and deployed, the simulation originally used was rather out of date. One of my first tasks was to update the geometry used in this simulation so that it was accurate to the final design of the prototype detectors.

All major elements of the geometry of the detector were simulated in this preliminary geometry. The cylindrical NaI crystal is placed at the origin, with the ends of the cylinder facing up and down along the z-axis. Cylindrical quartz light guides sandwich the crystal, allowing light to travel through while distancing the crystal from the radioactivity of the glass in the PMTs. These photoelectric tubes are implemented in a few segments: base, body, and cathode. (See engineering drawing 4.2 .)

In updating the simulation geometry, I made several changes. These changes include:

-replacing mineral oil with nitrogen gas

-adjusting dimensions of crystal and pressure vessel

-addition of copper rods

-addition of steel midplate

For a detailed description and picture of the current geometry for DM-Ice17, please see figure 5.1.

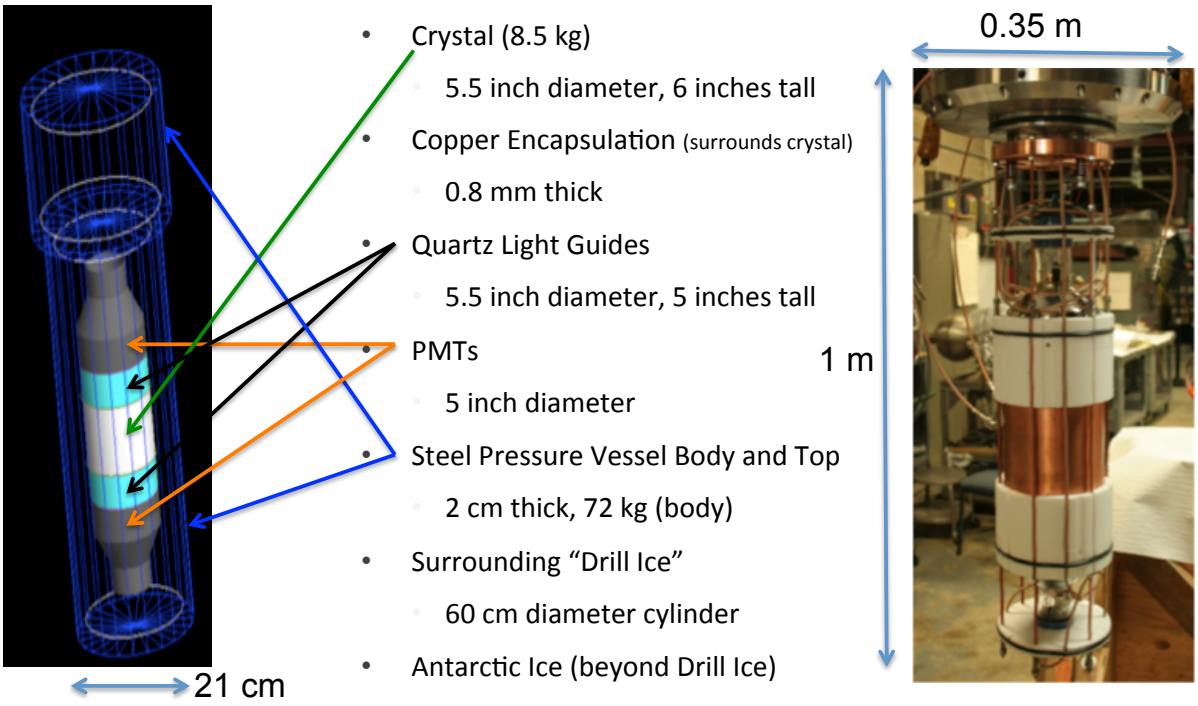


Figure 5.1: Simulated Geometry and Components of DM-Ice17. Also visible in the photograph are the white PTFE stabilizer rings, and the array of vertical copper rods which support the detector components. Please see table 6.7 for contamination levels in each component.

## 5.2 Physics List

Geant4 references physics lists in order to propagate and decay particles properly. These physics lists contain tables of data measured experimentally. A physics list contains information about particles, physics processes (such as scattering or radioactive decay), and production thresholds. Many physics lists exist for general use, although anyone can compile their own physics list if they wish. Some commonly used physics list include QGSP_INCLXX, QGSP_BIC_HP, FTFP_BERT, and many more variations. Each is optimized for a certain purpose (you may visit the Geant4 documentation online for further information on physics lists, and which applications for which each list is useful). Some are intended for use in

simulating collider physics, others for neutrino experiments, and others for medical physics applications, and many more. Usually this optimization involves a sort of tradeoff between level of detail and quickness of processing speed. Each experiment needs to decide what physics list is most suitable for their experiment.

For DM-Ice, we have used only physics lists created (and tested) by others, so that we know they are reliable, and for easier comparison to other results. Different physics lists are appropriate for different situations. Since we are focused on low energy when performing a dark matter search, we have primarily used the physics list "exrdmPhysicsList". This list contains primarily Livermore physics processes. We chose this physics list because it is used in example rdecay02, which had similar energy region and particle type priorities to DM-Ice (as opposed to the physics lists used by the LHC for high energy experimentation and simulation). I ran briefly with the "shielding" physics list in order to compare to the usual list when troubleshooting a decay problem. Physics list selection is a topic that will be revisited as we go on, to make sure we are using the most optimized and accurate version for our particular experiment and simulation.

### 5.2.1 Isotope Decays

Particles can be placed at a particular location within the geometry (inside or outside the detector itself) and then allowed to propagate. Particles can be given an initial energy/momentum. A stable particle will propagate in space and time as it would in the actual detector. A radioactive particle can be placed either with kinetic energy/momentum or be at rest. For the DM-Ice simulation, particles are placed at rest in order to simulate the decay of radioactive nuclei within the materials of and surrounding the detector. This is because the most significant anticipated backgrounds are from the crystal and detector components, as opposed to particles coming from the surroundings, due to the excellent shielding properties of the ice. These nuclei then decay, and the decay products are tracked. If a daughter nucleus is created, which then decays itself, a chain of decays and decay products is created, and all resulting particles are then tracked and recorded.

Particles can also be distributed throughout a volume. For instance, instead of running a certain number of $^{40}$K decays at one location in the steel pressure vessel, Geant4 can be instructed to evenly distribute these decays throughout the whole pressure vessel volume. This allows us to simulate the actual situation of the radioactive contaminants in our detector.

## 5.3 Simulation Verification

$^{60}$Co provides a convenient first check on Geant4 simulation results. Its most notable peaks are at 1170 and 1333 keV. This is also the isotope which was used to calibrate the crystals at Boulby, and therefore comparison among pre-deployment calibration data, in-ice data, and simulation provided useful information for detector calibration. When run in the crystal, these peaks are easily seen. This indicates that the package is working properly, at least to first order. $^{40}$K is also a convenient option to verify things are working correctly; a $^{40}$K spectrum may be seen in Chapter 6. Alpha locations are another useful check, looking at $^{238}$U and $^{232}$Th chains, but beta shoulders and x-ray peaks are also important to check. These have all been verified and checks have been made regarding propagation and radiation length/attenuation length to check reasonableness of results.

## 5.4 Selecting backgrounds

Distributing decays throughout volumes is well and good, but what rate is needed to replicate what is seen in our detector? The materials used are not pre-measured, so that upon assembling and deploying DM-Ice17, we did not have data available on exact levels of contamination.

### 5.4.1 Measurements

Several materials were explicitly measured at SNOLAB. Steel (pressure vessel), drill ice, optical gel, PTFE supports. These measurements either come with error bars or are simply an upper limit. While I tweaked these values considerably from time to time, in the end for

our paper [40], we took the "central" value of the measurements. Broken (out of equilibrium) chains were observed in this SNOLAB data. and are noted in table 4.1.

Several materials have unknown exact contamination levels, and we have been unable to measure them directly (quartz light guides, PMT, crystal). The PMTs have a data sheet that we referenced, but since they were manufactured a while back, it's unknown whether the data sheet is exactly accurate. The quartz we have an idea of what might be reasonable contamination levels, but no exact figures at all. The NaI crystals have been characterized in a few ways during their time as NAIAD detectors but their contamination levels were never measured that we are aware of. We do know that they are significantly dirtier than the crystals used by DAMA.

### 5.4.2 Simulation and Data

For these components of unknown contamination, I have used a crude "by eye" fitting method to estimate the contamination levels. First, I determined what seemed to be a reasonable level of contamination for each component based on various resources (datasheets, etc) and measurements of similar materials (ILIAS [2] and others). Then I simulated those components using those levels, and plotted the resulting spectrum against the data spectrum (see Chapter 6). By looking at particular peaks and shoulders, I determined whether these estimates seemed to be too high or too low for each contaminant in each material, and corrected accordingly.

This method was particularly essential in the alpha region of the spectrum ($\approx$ 2-5 $MeV_{ee}$). The relative heights of these peaks allowed an estimate of the $^{238}U$ and $^{232}Th$ chain contaminations in the crystal, as well as information on each segment of their broken chains (see table 6.4). This estimate was then used in the beta/gamma energy region plots ($\approx$ 0-2 MeV) since there are no distinguishing features for $^{238}U$ and $^{232}Th$ in the crystal in this region.

## 5.5 Matching to data

Once matched to data, these estimates were again verified to be reasonable for the materials present. These levels were used in the simulation plots in our paper [40]. See figures in Chapter 6 to see how well data and simulation agree.

## 5.6 Simulation Overview

Simulation provides a key insight into both understanding our detector and planning for the next phase of the experiment. Chapter 6 will continue discussion of simulation in the context of data from DM-Ice17.

# Chapter 6

# Comparison of Simulation with DM-Ice17 Data

## 6.1 Plotting from simulation: ROOT

ROOT is a plotting package created by the LHC collaboration at CERN. Geant4 conveniently outputs simulated events into a ROOT file which can then be plotted as a histogram using the ROOT package.

## 6.2 Matching to data

The background simulation is intended to represent the radioactive contamination of the detector. A number of components of the detector have been measured, so that we know what their contamination levels are for various isotopes. Other components are not known, although we have an idea of the general range of amounts and types of backgrounds which would be typical for that material. For the measured components, I simply take the activity rate for each isotope, and (having already run sufficient statistics of each isotope in each material) scale the contribution to mimic what we see in the actual detector. If all components had been measured, I would do this for every component and every isotope, and then we would expect the compiled simulation to match the data from DM-Ice17.

### 6.2.1 Levels set by "fitting" to data

Since we do not know all of the levels of contamination, we do a bit of matching or fitting between simulation and data. I began with the alphas. Peaks for the various alpha particles expected in the NaI crystal have known energies. This allows me to simulate the $^{232}$Th and

$^{238}$U chains in the crystal, and then scale the amounts in order to match what we see in the data. There are no contributions to these alpha peaks from outside the crystal, since the range of alpha particles in matter is so small. This scaling has been done by eye, and it remains for future work to improve the fit by using an actual fitting function to determine the contributions from each alpha peak. What has been done is sufficient for the present purpose, and is estimated to be accurate to about 30%. These results for alphas are shown in table 6.4.

### 6.2.2 Alpha Quenching

Electron equivalency/electron equivalent energy is what we usually think of, but the alphas are actually quenched. This quenching factor refers to the fact that only about half of the energy of a given alpha particle will be detected in the crystal. This is due to a reduced scintillation efficiency for alphas. Quenching is reported via a comparison of the true energy of the alpha and what is visible in the crystal. $E_{nr}$ (nuclear recoil) and $E_{ee}$ (electron equivalent) reflect quenched and unquenched energies as well.

The quenching factor in DM-Ice17 has been estimated by comparing simulation to data; see equation 6.4. DAMA gives a quenching factor in their paper (see equation 6.1 ), as well as posted plots of several alpha sections of their crystals (see figure 6.1 ). I used the DAMA alpha plots to practice estimating quenching factors from plots, and got answers quite similar to theirs as reported in the paper. I then used the same general method to estimate the DM-Ice17 quenching factors. I found that in order to get good agreement, I had to use two terms in the relationship, as DAMA does. Other references which quote quenching factors usually quote a single term, with no energy-dependent term. DAMA does not explain why they use this method, but it seems to fit their published alpha plots well, and also fits our data quite well.

| **Material** | **Reference** | **Link** |
|---|---|---|
| Crystal ($^{238}$U, $^{232}$Th) | Simulation alpha analysis | Section 6.3.3, table 6.4 |
| Crystal ($^{40}$K) | Beta shoulder | Section 6.4.1, table 6.4 |
| Quartz | ILIAS Radiopurity Database (Silica Rod) | http://hepwww.rl.ac.uk/ukdmc/radioactivity/uk.html |
| PMT | ET Enterprises 9390KB 5” | http://icecube.wisc.edu/~breilly/researcharea/9390KB.pdf, Figure 6.9. |
| Steel | SNOLAB measurements | Table 4.1 |
| Drill Ice | SNOLAB measurements | Table 4.1 |

Table 6.1: DM-Ice-17 Contamination references

## 6.3 Alpha Analysis

### 6.3.1 Overview and Goals

The alpha region of the background spectrum for NaI detector was simulated, and then compared to DAMA's published results and DM-Ice17 spectrum. Estimates of contamination of $^{238}$U and $^{232}$Th in the NaI crystal were obtained, including different portions of the $^{238}$U chain since the chain is not in equilibrium. Estimates of quenching factors were also obtained, and it was determined that these may vary from crystal to crystal to some extent. Energy resolution is considered as well. Since we need to reproduce via simulation both the amounts of alpha contamination as well as the quenching factor, a test case was desirable. DAMA has published images of their alpha regions for several crystals as well as a quenching factor for a typical crystal [4]. Therefore, I first compared my simulation to DAMA's results to test whether I could reproduce their results accurately. Once I confirmed I could extract contamination levels from comparing alpha data with simulation, I used this process to estimate the $^{238}$U and $^{232}$Th content of the DM-Ice17 crystals.

### 6.3.2 Analysis of DAMA alphas

DAMA quotes contaminations of 0.7-10 ppt $^{238}$U in NaI crystal and 0.5-7.5 ppt $^{232}$Th in NaI crystals.

DAMA reports that the $^{238}$U chain is not in equilibrium but broken into five pieces (see table 6.2). Decay rates are also provided by DAMA for the "d" crystal (see figure 6.1), both for the broken $^{238}$U chain and the $^{232}$Th chain.

| Chain portion isotopes | Chain portion number | Chain portion rate |
|---|---|---|
| $^{238}$U-$^{234}$Pa | (1) | 4.4 uBq/kg |
| $^{234}$U | (2) | 15.8 uBq/kg |
| $^{230}$Th | (3) | 15.8 uBq/kg |
| $^{226}$Ra-$^{214}$Po | (4) | 21.7 uBq/kg |
| $^{210}$Pb-$^{206}$Pb | (5) | 24.2 uBq/kg |
| ($^{232}$Th) | (-) | (8.5 uBq/kg) |

Table 6.2: DAMA crystal d broken $^{238}$U chain and $^{232}$Th rates; taken from paper [4]

#### 6.3.2.1 DAMA plots introduction

In figure 6.1, 5 distinct peaks are resolved from the alphas (as shown in figure 6.2). These alphas come from the $^{238}$U and $^{232}$Th chains, and are accounted for in the peaks as in table 6.3:

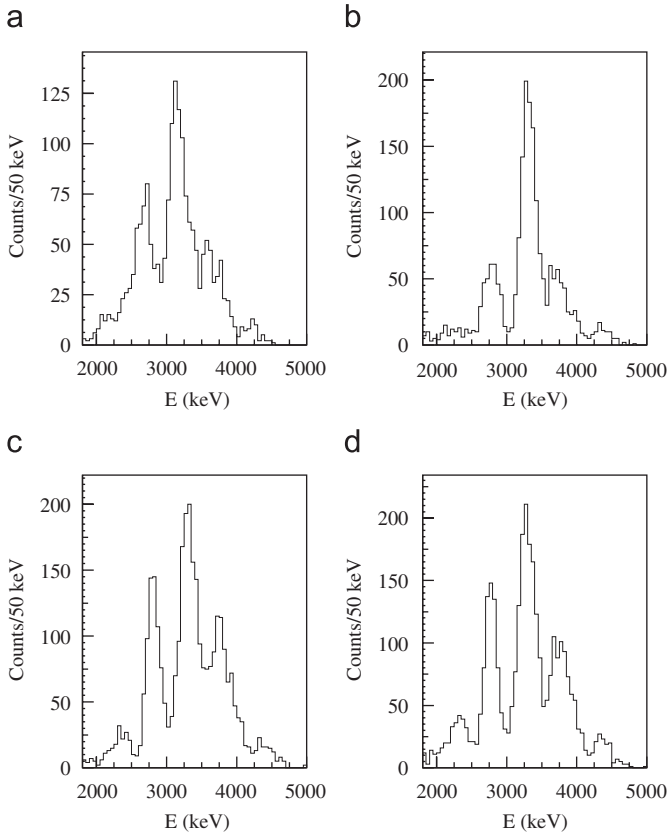


**Fig. 8.** The $\alpha$ energy distributions in some of the NaI(Tl) crystals corresponding to a live time of 570 h. The energy is given in keV electron equivalent.

Figure 6.1: DAMA has published alpha spectra from four of their crystals [4]. These spectra are shown in electron equivalent units (quenched energy), and were used in order to test the alpha contamination estimation process using the DM-Ice simulation.

### 6.3.2.2 DAMA plots (d) and (c) with simulation

In figure 6.4, plots (a) - (d), I have simulated the same concentration over the same period of time as DAMA (570 hours). The binning is the same (50 keV/bin).
DAMA quotes their quenching factor (cited for crystal "d") in equation 6.1 as:

$$\text{alpha/beta} = 0.467 + 0.0257 \times \text{E}_\alpha \tag{6.1}$$

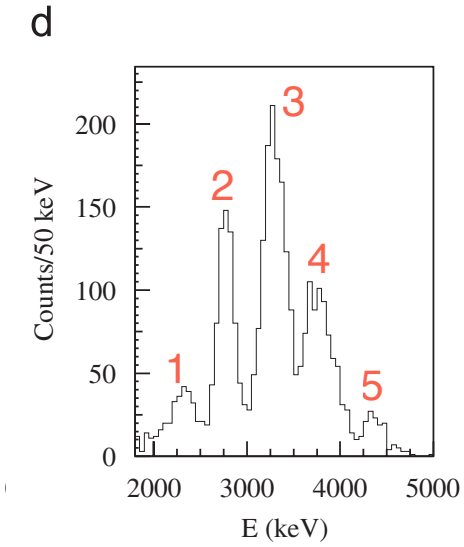


Figure 6.2: DAMA alphas, peaks labeled for reference (see table 6.3 ) [4]

| Peak ID | Contributing isotopes |
|---|---|
| peak 1 | $^{232}$Th$^{\dagger}$, $^{238}$U* |
| peak 2 | $^{234}$U*, $^{230}$Th*, $^{226}$Ra* |
| peak 3 | $^{210}$Po*, $^{228}$Th$^{\dagger}$, $^{222}$Rn*, $^{224}$Ra$^{\dagger}$ |
| peak 4 | $^{218}$Po*, $^{212}$Bi$^{\dagger}$, $^{220}$Rn$^{\dagger}$ |
| peak 5 | $^{216}$Po $^{\dagger}$ |
| | |

Figure 6.3: Alpha peak components; Peak ID as in figure 6.2. A $^{\dagger}$ indicates isotope is a member of the $^{232}$Th chain; * indicates a member of the $^{238}$U chain.

Equation 6.2 shows a modified version of DAMA's quenching factor:

$$\text{alpha/beta} = \mathbf{0.45} + 0.0257 \times \mathrm{E}_{\alpha} \tag{6.2}$$

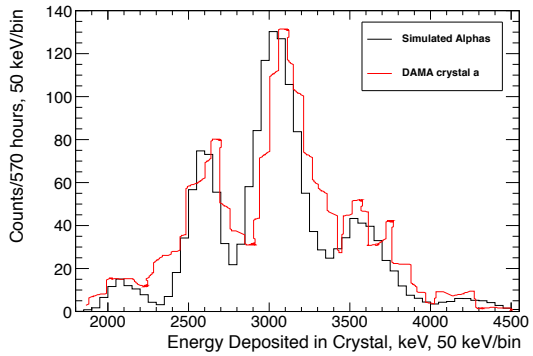


(a)

Simulated alpha energies in simulation are quenched according to equation 6.3

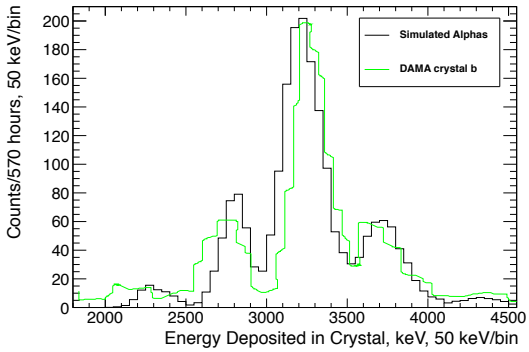


(b)

Simulated alpha energies in simulation are quenched according to equation 6.2

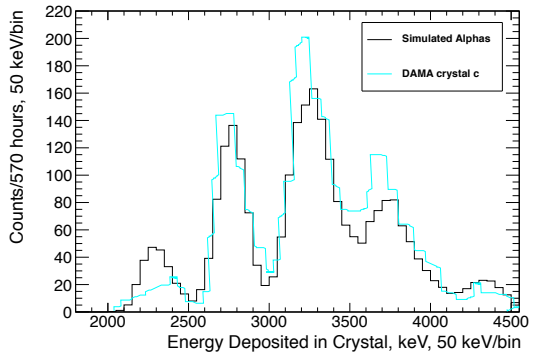


(c)

Simulated alpha energies in simulation are quenched according to equation 6.3

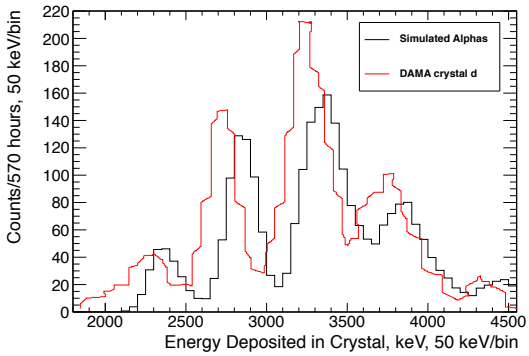


(d)

Simulated alpha energies in simulation are quenched according to equation 6.1

Figure 6.4: DAMA plots (a) - (d) and simulation adapted to match each. Concentrations of $^{238}$U chain (broken) and $^{232}$Th chain (equilibrium) are used in simulation as shown in table 6.2. Alpha energies in simulation are quenched according to the equations found in table 6.5. (*Quenching is implemented in simulation after running a number of decays, at the time of creating the plots.)

#### 6.3.2.3 DAMA plots (b) and (a) with simulation

For DAMA plots (a) and (b) 6.1 I found that the $^{238}$U chain was broken differently than quoted by DAMA. This means that the intensities or rates from the portions of the chains were different, not that the chain broke in different places, since the places the chain breaks is related to half-lives and not anything that can vary from crystal to crystal. See figure 6.3 for the numbers on how the $^{238}$U chain broke in these DAMA crystals. Note that these numbers were obtained by changing different peak heights by hand and eyeballing the result to see if it matched up with DAMA's plot. I got much better agreement with these numbers than with DAMA's (d) numbers, but they are not necessarily a highly precise answer.

With regard to quenching for DAMA's (a) plot, neither equation 6.1 nor equation 6.2 gave very good agreement between simulation and DAMA's plot. So I changed 6.1 further, to the form shown in equation 6.3:

$$\text{alpha/beta} = \mathbf{0.35} + \mathbf{0.038} \times \mathrm{E}_{\alpha} \tag{6.3}$$

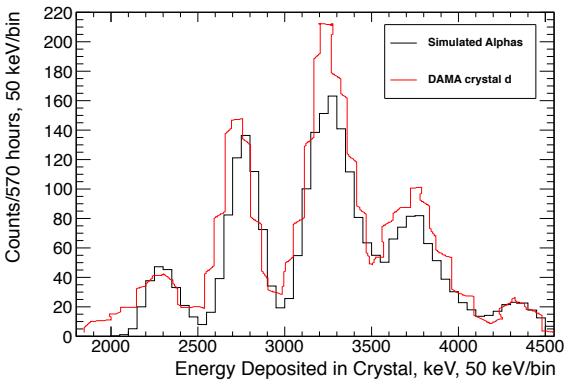


Figure 6.5: DAMA alpha plot (d) with quenching factor modified (see equation 6.2) from value quoted in [4] (see equation 6.1 ). Included for completeness; since DAMA quotes this quenching factor specifically, I will generally use their value when referring to this crystal, but thought it important to include this modification since it matches rather better.

| Chain portion isotopes | Chain portion number | Chain portion rate (a) | Chain portion rate (b) |
|---|---|---|---|
| $^{238}$U-$^{234}$Pa | (1) | 1.089 uBq/kg | 0.311 uBq/kg |
| $^{234}$U | (2) | 10.89 uBq/kg | 9.33 uBq/kg |
| $^{230}$Th | (3) | 10.89 uBq/kg | 9.33 uBq/kg |
| $^{226}$Ra-$^{214}$Po | (4) | 17.4 uBq/kg | 15.5 uBq/kg |
| $^{210}$Pb - $^{206}$Pb | (5) | 28.3 uBq/kg | 46.65 uBq/kg |
| ($^{232}$Th) | (-) | (3.55 uBq/kg) | (5.08 uBq/kg) |

Table 6.3: DAMA (a) and (b) $^{238}$U chain (broken) and $^{232}$Th (equilibrium) rates

### 6.3.3 Alpha Simulation and DM-Ice17

Once I was confident the simulation was working properly and that I knew how to adjust broken chain intensities and quenching factors, I moved on to looking at the alpha spectrum of DM-Ice17. When I did the DAMA fitting as above, I left $^{232}$Th in equilibrium (as DAMA did). I found later that I was able to better match simulation and data if I broke the $^{232}$Th chain into two sections (see tables 6.4 and 6.6 ). Simulation of DM-Ice17 alpha (and beta/gamma as well) regions therefore has this in effect while the simulations used for DAMA comparisons do not. Analysis of DM-Ice17 alpha region allows values to be extracted for the $^{238}$U and $^{232}$Th decay chains, as described below.

$$\begin{aligned} \text{Quenching Factor for Det-1:} \quad & \text{alpha/beta} = \mathbf{0.435} + \mathbf{0.039} \times \mathrm{E}_{\alpha}(MeV) \\ \text{Quenching Factor for Det-2:} \quad & \text{alpha/beta} = \mathbf{0.47} + \mathbf{0.034} \times \mathrm{E}_{\alpha}(MeV) \end{aligned} \tag{6.4}$$

### 6.3.4 Alpha Analysis Summary

DAMA's stated quenching factor appears to roughly match the corresponding alpha plot they have published (d), but small modifications seem to provide better agreement between the Geant4 simulation and DAMA's data. Modifying the quenching factor further permits

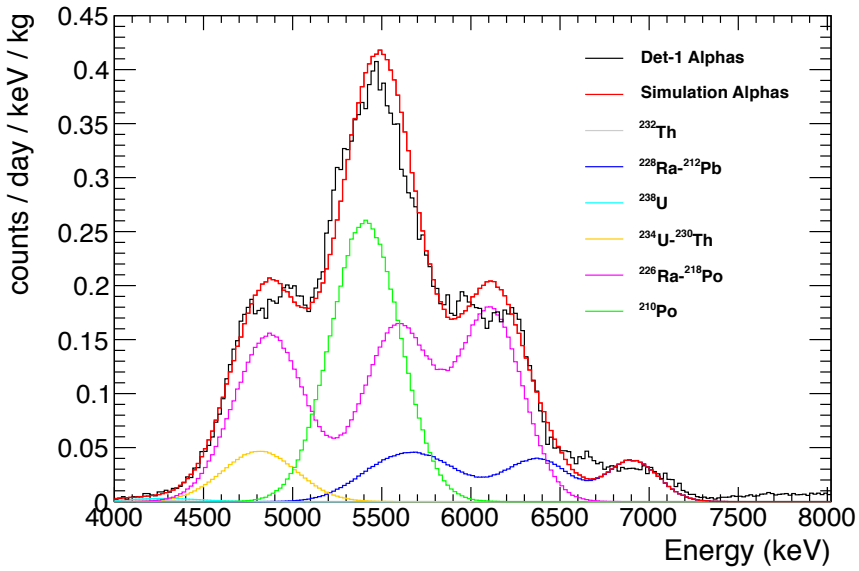


Figure 6.6: DM-Ice-17 data (Prototype 1) and simulation. Binning is 20 keV/bin for both simulation and data. Concentrations of $^{238}$U chain (broken) and $^{232}$Th chain (broken) are used in simulation as shown in tables 6.7 and 6.4. Quenching factor for Det-1 alphas is shown in equation 6.4. Energy resolution percentage varies from 5 to 1 as energy increases, according to equation 6.5. These alpha energies are not quenched. (the simulated particles have not had a quenching factor applied, and the data has had the quenching factor applied inversely in order to "unquench" the energies for comparison to simulation.)

good agreement between simulation and DAMA data for their other published alpha plots (a), (b), (c).

DM-Ice17 comparison of alpha data and alpha simulation allows for an estimation of quenching factor in the same way. The quenching factor which facilitates good agreement between simulation and DM-Ice17 data conforms to the same pattern as the DAMA quenching factors, and has similar values. Thus, we have estimated the quenching factors of DM-Ice17, and feel confident that these results are reasonable.

The quenching factor values are gathered in table 6.5.

The alpha simulation analysis also permits estimation of the contamination content of the DAMA and DM-Ice17 crystals. As with the quenching factor, DAMA has given values for the radioactive contamination of one of its crystals (d) [4]. Simulation of these contamination levels confirms that these numbers give fairly good agreement with data. The simulation then also allows extraction of similar contamination levels for the other DAMA crystals for which we have plots: (a), (b), and (c). It is found that (c) is very similar to (d), so no separate values are reported, but the levels for (d), (b), and (a) are listed in table 6.6.

Having confirmed the ability of the simulation to estimate contamination content of crystals by examining the alpha spectrum, the DM-Ice17 alpha spectrum was examined. The extracted values for crystal contamination due to $^{238}$U and $^{232}$Th chains are our sole estimates of these levels, which are our primary background in the region of interest. Understanding the internal contamination of the crystal is therefore of the utmost importance, and this alpha analysis allows an estimate without which we would have a severe handicap when examining the low-energy region, where a dark matter signature may be seen or excluded. Internal contamination numbers for DM-Ice17's NaI crystals can be found in table 6.4. A rough comparison of the contamination levels found in DAMA crystals as in [4] and DM-Ice17 can be found in table 6.6 .

Alpha analysis led to the broad conclusion that the DM-Ice-17 crystals seems to be about $\mathbf{10-50}$ times dirtier than DAMA's crystals on average, of the ones for which they provided alpha plots (see table 6.6). This result of order 10 or 100 difference between the DM-Ice17 and DAMA crystals was an important early conclusion for the DM-Ice project. This implied that if these (relatively dirty) older crystals were even this close to DAMA purity levels, we could likely procure crystals clean enough for our purposes for the full-scale DM-Ice detector. These numbers also informed us what sort of constraints on our results with DM-Ice17 would be like, given the degree of contamination in the crystals. In addition, knowing the contamination of our crystals was essential in order to simulate the gamma and beta energy regions, and especially the region of interest. Since DM-Ice17 was not calibrated with

any external source, these alpha lines are our only handle on measuring the crystal internal contamination.

$^{238}$U: 1 Bq/kg = 81 ppb

$^{232}$Th: 1 Bq/kg = 246 ppb

$^{40}$K: 1 Bq/kg = 32.3 ppm

Figure 6.7: Conversion between Bq/kg and ppb for $^{238}$U and $^{232}$Th in equilibrium, and $^{40}$K:

| Isotope | Subchain | Activity (mBq/kg) |
|---|---|---|
| $^{40}$K | | 17 |
| $^{129}$I | | 1 |
| $^{232}$Th | $^{232}$Th | 0.01 |
| | $^{228}$Ra – $^{208}$Tl | 0.16 |
| $^{238}$U | $^{238}$U – $^{234}$Pa | 0.017 |
| | $^{234}$U – $^{230}$Th | 0.14 |
| | $^{226}$Ra – $^{214}$Po | 0.90 |
| | $^{210}$Pb – $^{210}$Po | 1.5 |

Table 6.4: Contamination in the NaI crystals as determined by simulation comparison to data spectral features (see figure 6.6). The activity levels in the two detectors are consistent within the $\approx 30\%$ error of these numbers. Both $^{238}$U- and $^{232}$Th-chains were observed to be broken. The value for $^{129}$I was taken from ANAIS's measurements of its crystals, and kept the same since it matched data well [5] .

| **Crystal ID** | **Quenching Equation** |
|---|---|
| DAMA (d) | $E_\alpha/E_\beta = 0.467 + 0.0257 \times E_\alpha$ |
| DAMA (c) | $E_\alpha/E_\beta = 0.45 + 0.0257 \times E_\alpha$ |
| DAMA (b) | $E_\alpha/E_\beta = 0.45 + 0.0257 \times E_\alpha$ |
| DAMA (a) | $E_\alpha/E_\beta = 0.35 + 0.038 \times E_\alpha$ |
| DM-Ice17 | $E_\alpha/E_\beta = 0.435 + 0.039 \times E_\alpha$ |

Table 6.5: Quenching Equations for various crystals (all energies in MeV). DAMA (d) crystal is taken from their apparatus paper [4]; the other quenching factors are derived from comparing data and simulation.

| Isotopes | Subchain | DAMA d | DAMA b | DAMA a | DM-Ice-17 | DM-Ice/DAMA |
|---|---|---|---|---|---|---|
| $^{238}$U-$^{234}$Pa | (1) | 4.4 uBq/kg | 0.311 uBq/kg | 1.089 uBq/kg | 17 uBq/kg | 9 |
| $^{234}$U | (2) | 15.8 uBq/kg | 9.33 uBq/kg | 10.89 uBq/kg | 140 uBq/kg | 12 |
| $^{230}$Th | (3) | 15.8 uBq/kg | 9.33 uBq/kg | 10.89 uBq/kg | 140 uBq/kg | 12 |
| $^{226}$Ra-$^{214}$Po | (4) | 21.7 uBq/kg | 15.5 uBq/kg | 17.4 uBq/kg | 900 uBq/kg | 50 |
| $^{210}$Pb - $^{206}$Pb | (5) | 24.2 uBq/kg | 46.65 uBq/kg | 28.3 uBq/kg | 1500 uBq/kg | 45 |
| ($^{232}$Th) | (-) | (8.5) uBq/kg | (5.08) uBq/kg | (3.55) uBq/kg | (160 uBq/kg) | 28 |

Table 6.6: Intensity levels for broken U chain and $^{232}$Th. (lower portion or subchain of $^{232}$Th only was used) The DM-Ice-17 crystals seems to be about $\mathbf{10-50}$ times dirtier than DAMA's crystals on average, of the ones for which they provided alpha plots. [Note that this table reports the $^{232}$Th chain as in equilibrium, or unbroken. Further alpha analysis revealed better data-simulation agreement when this chain is broken, as in table 6.4. For purposes of this table, only the value for the lower portion of the chain is reported.]

## 6.4 Gamma/Beta analysis

Having used the alpha analysis to estimate the internal contamination of the crystal, the next step is to consider the 0-2 MeV range of the energy spectrum. With many free variables in this section from unmeasured components, it's essential to pin down as many as we can. Several components were measured at SNOLAB, as discussed 4.3.2, and the $^{238}$U and $^{232}$Th crystal contaminations are set by the alpha analysis. Particular features in the spectrum (see table 6.8 ) as well as general knowledge about contamination levels in similar materials were then used to estimate the contamination of the remaining unmeasured components.

In order to determine the best match between simulation and data, and set estimates of contamination levels, some starting point had to be chosen. The overall energy spectrum was expected to have significant contributions from the crystal, the quartz light guides, the PMTs, the stainless steel pressure vessel, and possibly the drill ice. The steel and drill ice have been measured at SNOLAB 4.3.2. Estimates of contaminations in the other materials were needed; they were taken from a few different locations. The levels for the PMTs were based on a datasheet (see figure 6.9 ) for the same model PMT (though not necessarily identical to the PMTs used in DM-Ice17), the quartz was based on measurements of clean quartz found in the ILIAS database [2] (although the particular variety of quartz used in DM-Ice17 is unknown), and the $^{238}$U and $^{232}$Th levels of the crystal were estimated from the alpha analysis described above. $^{40}$K in the crystal was originally estimated to be in similar relative proportions to $^{238}$U and $^{232}$Th as reported by DAMA, and then estimated more specifically based on the $^{40}$K beta shoulder.

| **Isotope** | **Location(s)** | **Feature/Peak** | **Parent Chain, if applicable** |
|---|---|---|---|
| $^{214}$Pb | Quartz, PMTs, Pressure Vessel | 352 keV peak | $^{238}$U |
| $^{214}$Pb | Quartz, PMTs, Pressure Vessel | 1765 keV peak | $^{238}$U |
| $^{214}$Pb | Quartz, PMTs, Pressure Vessel | 2204 keV peak | $^{238}$U |
| $^{214}$Bi | Quartz, PMTs, Pressure Vessel | 609 keV peak | $^{238}$U |
| $^{208}$Tl | Quartz, PMTs, Pressure Vessel | 2615 keV peak | $^{232}$Th |
| $^{60}$Co | Pressure Vessel | 1170 keV peak | N/A |
| $^{60}$Co | Pressure Vessel | 1370 keV peak | N/A |
| $^{40}$K | Crystal | Beta shoulder, Q = 1311 keV | N/A |
| $^{40}$K | Quartz, PMTs, Pressure Vessel | 1460 keV peak | N/A |
| $^{40}$K | Crystal | $\sim$ 3 keV | N/A |
| $^{210}$Pb | Copper Casing (inner surface, 10 micron depth) | $\sim$15 keV peak | $^{238}$U; only simulated from $^{210}$Pb down |
| $^{210}$Pb | Crystal | 46.5 keV peak | $^{238}$U |

Figure 6.8: Gathered a few of the most significant gamma and beta features in the spectrum. "Location" column often does not include the crystal, because many features do not appear in the spectra of isotopes decaying within the crystal. This is because not only the x-ray or gamma will be detected by the crystal (as may be the case if the decay originates from outside the crystal), but also the beta, or also accompanying photons. This means many distinguishable features originate only from outside the crystal. See figure 6.12, and note the shape of the crystal contribution to the spectrum. (The 3 keV feature is similarly often combined with other decay products, but sometimes the accompanying 1460 keV gamma escapes the crystal, leaving only the 3 keV x-ray to be detected. Since this occurs exactly in our region of interest, this feature is of particular interest.) On the whole, each of the features in this table should be visible in figure 6.12 (aside from the 3 keV peak; for this feature, see figure 6.13 ). Note that the double horizontal line separates features visible on the beta/gamma region of the spectrum from those visible in the low-energy region.

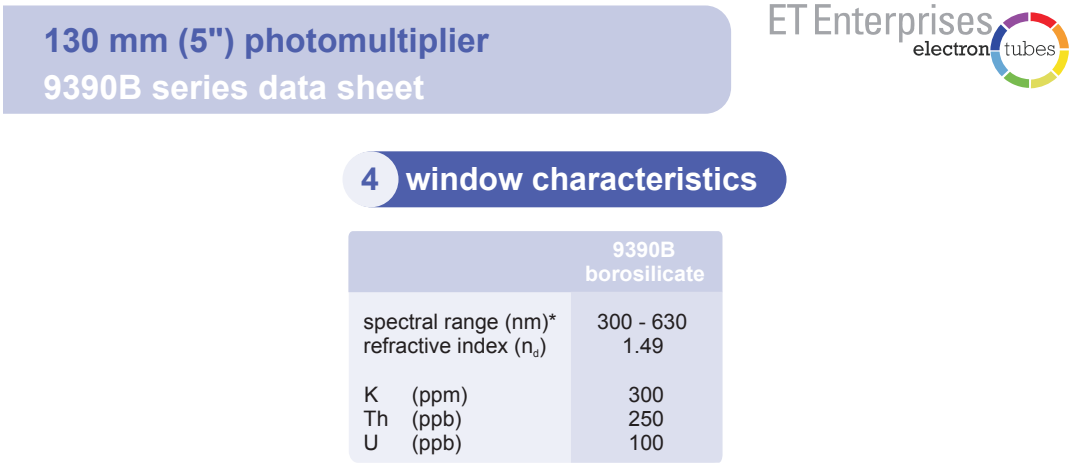

130 mm (5") photomultiplier
9390B series data sheet

ET Enterprises electron tubes

4 window characteristics

| | 9390B borosilicate |
|---|---|
| spectral range (nm)* | 300 - 630 |
| refractive index ($n_d$) | 1.49 |
| K (ppm) | 300 |
| Th (ppb) | 250 |
| U (ppb) | 100 |

Figure 6.9: Excerpts from PMT Datasheet. These contamination levels were taken as a base from which we determined our best estimate of our actual PMT background levels for DM-Ice17.

### 6.4.1 $^{40}$K in the crystal

After establishing a reasonable starting point for all contaminations, the next order of business was to estimate the actual $^{40}$K contamination in the crystal. This background is crucial to understand for two reasons. First, the 3 keV peak which occurs x% of the time in this decay is a dominant background in our low energy region, the region of interest for dark matter nuclear recoil ($\approx$ 0-10 keV). Second, there is an opportunity for an important veto with a multiple crystal detector array, as used in DAMA and planned for the full-scale DM-Ice experiment. This veto involves both the 3 keV peak and a peak at 1460 keV occurring in x% of $^{40}$K decays. While the 3 keV count cannot escape the crystal in which it originated, the 1460 keV gamma may register in a nearby crystal. Thus, a coincidence veto can be used: any 3 keV count accompanied by a 1460 keV count in a neighboring crystal can be thrown out as background. This coincidence analysis can also be used to estimate the $^{40}$K contamination level in the crystal.

The overall spectrum from the crystal contamination in this energy region is dominated by the characteristic beta shape, but the 1460 keV peak from $^{40}$K is well-defined. It would be easy to use this peak to determine the amount of $^{40}$K in the crystal if we already knew the $^{40}$K levels in the quartz lightguides, steel pressure vessel, and PMTs. However, since we lack all but one of those measurements (that of the steel), the $^{40}$K levels in the crystal were estimated based on the beta shoulder. This broad feature is the foundation for all of the peak features. Adjusting the $^{40}$K levels in the crystal essentially shifts the whole spectrum up and down. I modified these levels until the smooth portions of the simulated spectrum between 400-600 keV and 700-1000 keV aligned well with data (see figure 6.12 for spectrum details in this region). See figures **??** and **??** for $^{40}$K spectrum details. Consideration of these factors led to the estimate of the DM-Ice17 crystal $^{40}$K contamination, as found in table 6.4 .

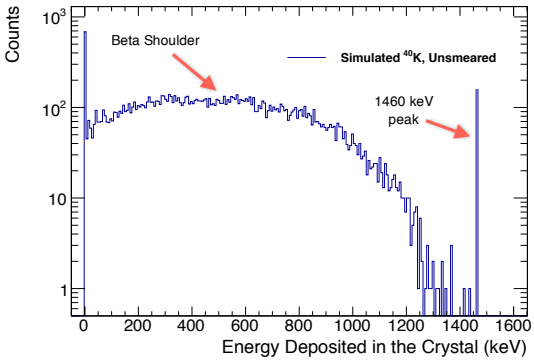


(a)

Spectrum produced by simulation (no energy resolution)

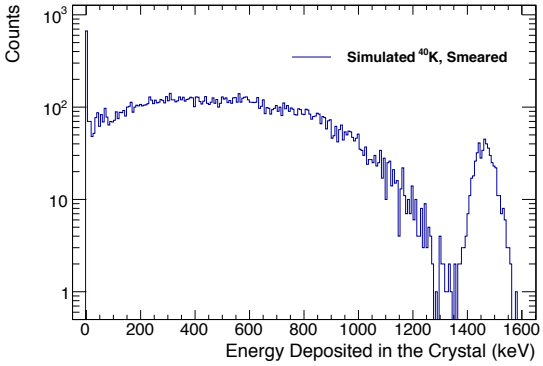


(b)

Simulated spectrum with energy resolution (smearing) according to equation 6.6 .

Figure 6.10: $^{40}$K in the crystal (internal contamination). 15,000 decays were simulated. The amount of $^{40}$K in the crystal was estimated based on the beta shoulder feature with endpoint energy 1311 keV. All simulation-data comparison plots have the simulation modified to approximate detector energy resolution.

### 6.4.2 609 keV peak considerations

The 609 keV peak from $^{214}$Bi was a significant focal point for matching simulation to data. This peak is relatively large and isolated, and so was a good reference point despite having two or three significant contributing regions. Once I more or less fixed the $^{40}$K level in the crystal, I began tinkering with PMT and quartz levels, with my eye on the 609 keV peak (in order to set the $^{238}$U levels for PMTs and quartz). The original estimate used in the simulation for quartz contaminations came from a PMT brochure (<5, <5, <5 ppb ppb ppm U/Th/K). In the end, we decided that the quartz was likely more comparable to the Spectrosil B quartz measured by ILIAS than the dirtier estimate we had originally started with. This left the major contributions to the 609 peak coming from the steel pressure vessel (whose $^{238}$U had been measured by SNOLAB), and the PMTs. This therefore allowed a first-order estimate of the $^{238}$U level in the PMTs. It turns out that the level found in the datasheet for the PMTs were fairly consistent with what we see in data, depending on which level of cleanliness is assumed in the glass. The low-background PMT glass is reported to have about 100 ppb of $^{238}$U, and the ultra-low background glass about 10 ppb. In the simulation, we found that about 30 ppb (or 2400 mBq/kg) fit best with data; somewhere in between the low-background and ultra-low background PMT reported values.

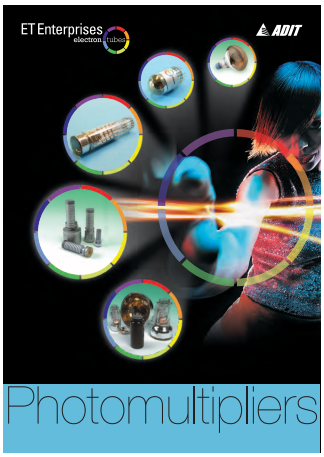


table 1

Background levels of elements containing radionuclides. Gamma decays per minute refer to a 50 mm diameter window of weight 30 g.

| material | K ppm | Th ppb | U ppb | total decays/ minute |
|---|---|---|---|---|
| standard borosilicate | < 60,000 | < 1000 | < 1000 | < 400 |
| low background | 300 | 250 | 100 | 25 |
| ultra-low background | 60 | 20 | 10 | 5 |
| quartz | < 5 | < 5 | < 5 | < 0.1 |

Figure 6.11: Excerpts from PMT Brochure. These quartz contamination levels were taken as an early estimate of the **quartz** contamination levels in DM-Ice17. Further investigation found that a better reference material was the Silica Rod B from the ILIAS UKDMC measurements. [2] `http://hepwww.rl.ac.uk/ukdmc/radioactivity/uk.html`

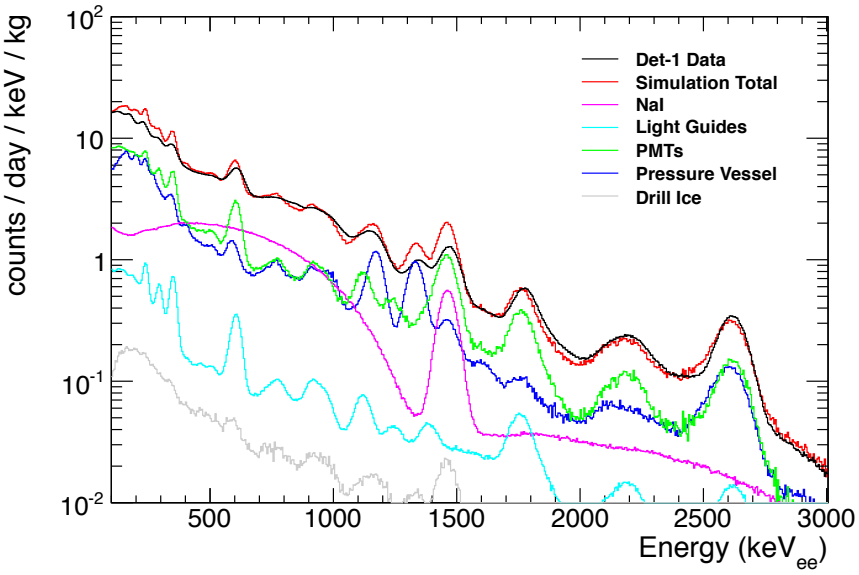


Figure 6.12: In order to estimate the contamination levels in the NaI crystal and other detector components and surroundings, a comparison of simulation to data was performed. Here is shown the 100 keV to 3000 keV region; alpha events have not been included (see figure 6.6 for alpha spectrum). This plot begins at 100 keV because that is the point at which our detector calibration switches; low-energy calibration is done separately from the "gamma region" calibration. In addition, the low-energy region (0-100 keV) is best considered when looking at a different data channel, ATWD0; for the portion of the spectrum above 100 keV, the channel ATWD1 is used. The difference between these channels as relates to these decisions involves better energy resolution at lower energies, and avoiding signal saturation at higher energies. For details on significant peaks, please refer to table 6.8. Contamination level estimates concluded from this simulation-data comparison can be found in table 6.7.

### 6.4.3 Low energy

The low-energy region is our region of interest for dark matter detection, and as such it is highly important that we understand our backgrounds in this region. This allows us to understand the behavior of the prototype detectors, and also to plan how best to build future detectors (materials, design, etc.) As you can see in figure 6.13, the primary features in this energy region are the 3 keV peak from $^{40}$K, the broad $\sim$ 15 keV peak from $^{210}$Pb, and the 46.5 keV peak, also from $^{210}$Pb. The 46.5 keV peak originates largely within the crystal, but the $\sim$ 15 keV peak must originate outside the crystal. We have determined that this peak is due to x-rays from $^{210}$Pb in the thin copper casing which surrounds the crystal to protect it from moisture. We note that it turns out that Geant4 will not simulate this peak unless the "Auger" option is enabled. No single x-ray is responsible for this peak, but rather several x-rays which can occur between approximately 10 and 20 keV. This results in the broader shape as seen in figure 6.13 . Since the 0-10 keV region is especially important, a zoomed-in version of this region has been included in figure 6.13 . As you can see, agreement between simulation and data is on the whole quite good. The 3 keV peak, which approaches our threshold for DM-Ice17, has a bit rougher agreement than the rest of the spectrum. This is due to processing the DM-Ice17 data in order to reduce noise: some of the signal is cut away as well, resulting in a smaller signal for the 3 keV peak in data than simulation. Accurate simulation of this peak is essential for estimating the actual contribution of this peak, since it is exactly in our primary region of interest.

To further comment on the $\sim$ 15 keV peak, it should be noted that in general, wherever $^{210}$Pb contributes to the simulated spectrum, it does so as one member of the $^{238}$U chain, which begins with the actual isotope $^{238}$U and continues down to the stable $^{206}$Pb. In order to reproduce the $\sim$ 15 keV as seen in 6.13, it was necessary to simulate only the portion of the $^{238}$U contained between $^{210}$Pb and $^{206}$Pb. The rationale for this is twofold: first, this is a valid breaking-point of the chain, due to the relatively long half-life of $^{210}$Pb (22.3 years); and second, it is known that $^{222}$Rn nuclei are prevalent in the air (especially in mines), and that these nuclei have been known to implant on surfaces exposed to air. We also wish to

note that the $^{210}$Pb (and daughters) were simulated only in the inner 10 microns (radially) of the copper case.

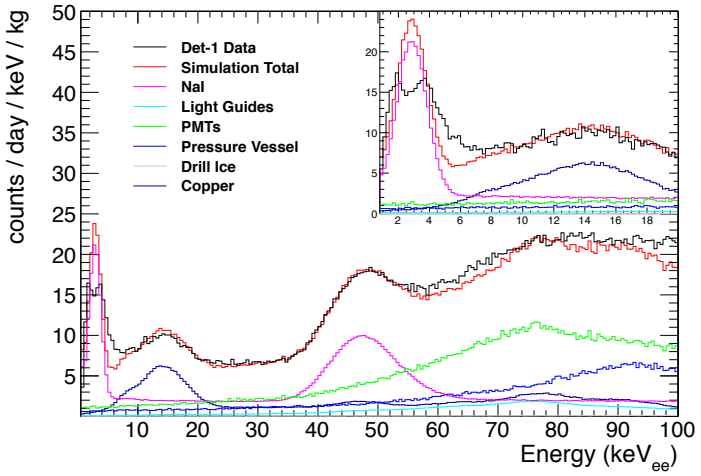


Figure 6.13: This is the comparison of simulation vs. data at low energies. Note good agreement across the entire energy range. Discrepancy between data and simulation for 3 keV peak is due to noise cuts on the data signal, resulting in loss of some signal. See text for further details.

**Low Energy Detail Plots** The low energy region of the spectrum is key for dark matter search. Please see figures 6.14, 6.15 and 6.16 for details of the significant contributions from the various regions and isotopes.

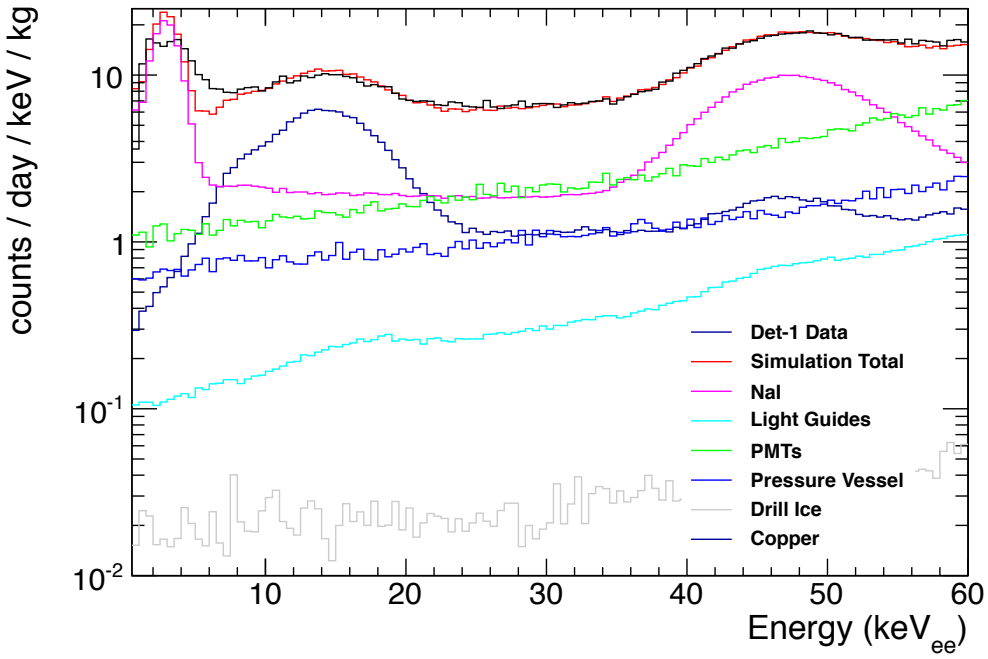


Figure 6.14: Detail of low energy region of simulation and data comparison shown by displaying the y-axis in log scale.

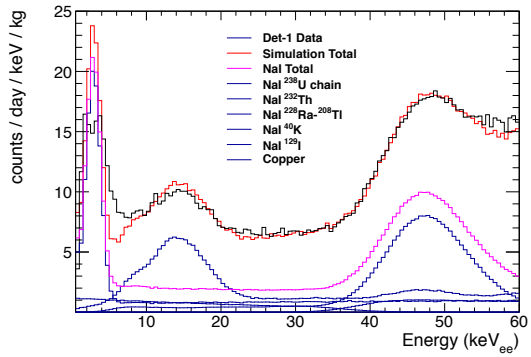


(a)

NaI crystal and copper encapsulation contributions.

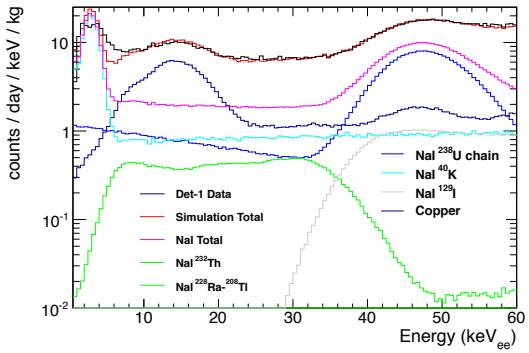


(b)

NaI crystal and copper encapsulation contributions.

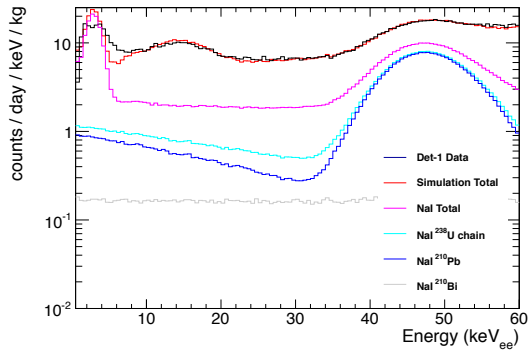


(c)

$^{238}$U chain contributions from those subevents which give higher rates from NaI crystal.

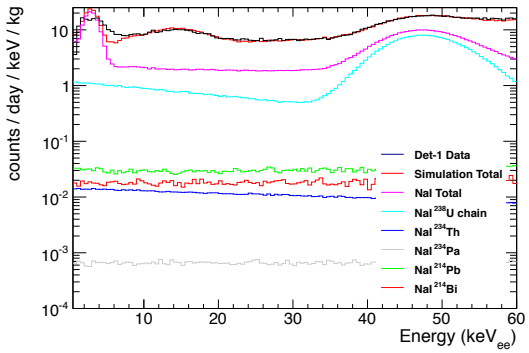


(d)

$^{238}$U chain contributions from those subevents which give lower rates from NaI crystal.

Figure 6.15: Details of low energy region of simulation and data comparison. Contributions from NaI crystal and copper encapsulation are shown individually.

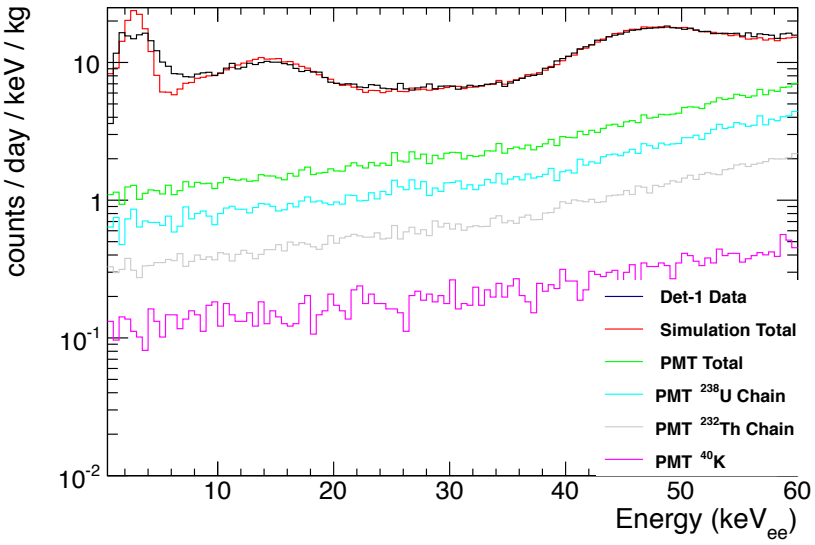


(a)

PMT contributions.

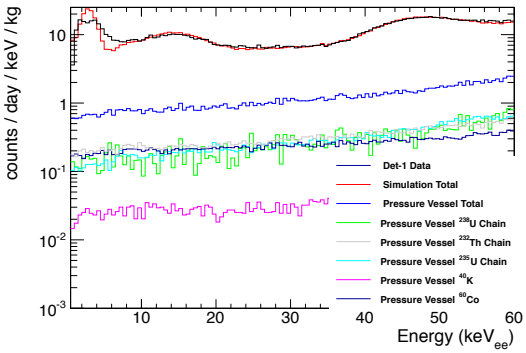


(b)

Pressure vessel contributions.

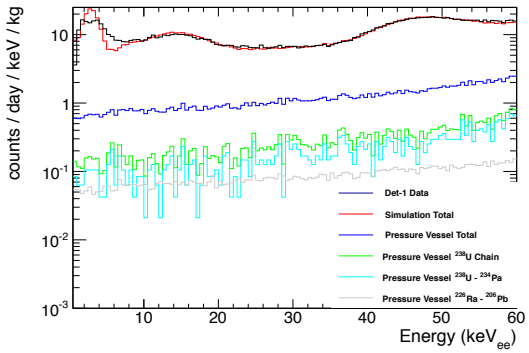


(c)

Pressure vessel $^{238}$U chain contributions.

Figure 6.16: Details of low energy region of simulation and data comparison. Contributions from PMTs and pressure vessel are shown individually.

### 6.4.4 Residuals

Subtracting data from simulation yields residuals, which give a visual reference for how well the two spectra agree. Figure 6.17 shows the residuals for each of the three energy regions.

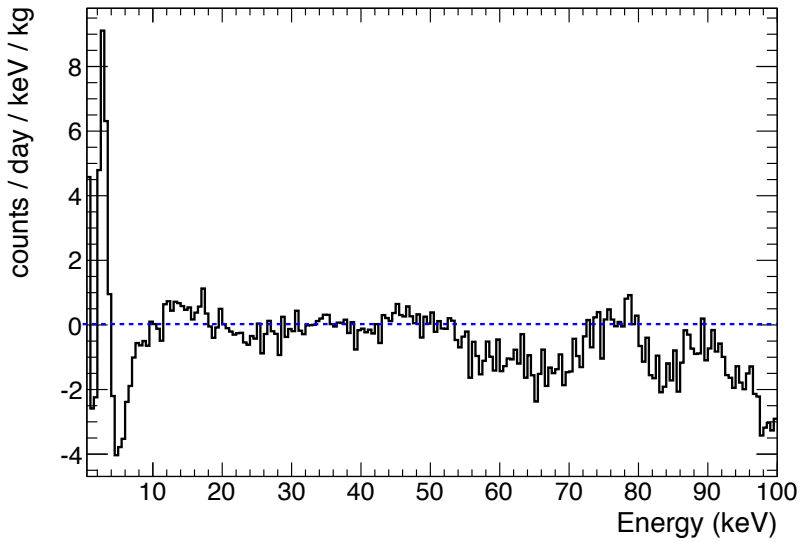


(a)

Low energy region residuals

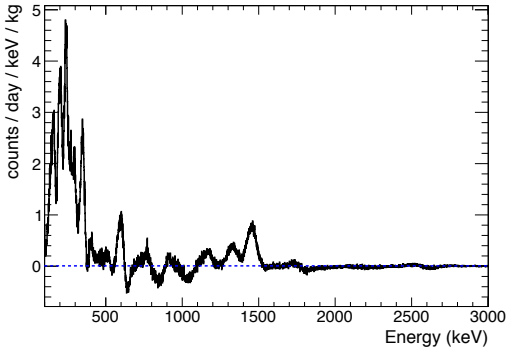


(b)

Gamma/Beta region residuals

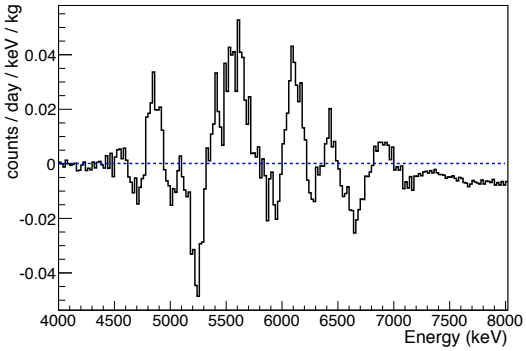


(c)

Alpha region residuals

Figure 6.17: Residuals of simulation-data comparison

## 6.5 Energy Resolution

Simulation records all energy deposited in the crystal, and reports each event's energy accurately. In real life, the detector has imperfect energy resolution. In order to approximate the energy resolution of the actual data in the simulated data, the simulation output has been "smeared." The simulated spectrum is convolved with a gaussian of appropriate shape, according to fits of the data to determine its energy resolution (which is energy dependent).

In the alpha region, a relatively simple energy resolution function allows simulation to match data quite well. The "Percent Energy Resolution" for the alpha region of DM-Ice17 is calculated as in equation 6.5 ; an energy resolution which depends linearly on the unquenched energy of the alphas provides good simulation-data agreement. When matching simulation to DAMA's alpha plots 6.1, I used an even simpler model. I simply imposed a 3% energy resolution in the simulation for comparison to each DAMA alpha plot, with the exception of DAMA's (a) plot, for which I used 3.5% energy resolution for better agreement between simulation and data.

When working with the beta/gamma region of the spectrum, a more complex relationship for determining energy resolution was used. Obtained by fitting the data spectrum, the energy resolution was found to be of the form $(\sigma/\mathrm{E})^2 = a/\mathrm{E} + b$ as in equation 6.6 .

$$\text{Percent Energy Resolution (Alpha region)} = -\mathrm{E}_{\alpha}^{unquenched,MeV} + 9 \tag{6.5}$$

$$\text{Energy Resolution (Gamma/Beta region)} : (\sigma/\mathrm{E})^2 = 0.317137/\mathrm{E} + 4.04886 \times 10^{-4} \tag{6.6}$$

## 6.6 Summary of simulation content

The Geant4 simulation of DM-Ice17 has permitted us to understand our detector's backgrounds and estimate specific levels for specific contaminations. These backgrounds are cataloged in table 6.7.

| Isotope/Region | Isotope | Rate (mBq/kg) |
|---|---|---|
| NaI | $^{40}$K | 17 |
| | $^{238}$U-$^{234}$Pa | 0.017 |
| | $^{234}$U | 0.14 |
| | $^{230}$Th | 0.14 |
| | $^{226}$Rn-$^{214}$Pb | 0.9 |
| | $^{210}$Pb-$^{206}$Pb | 1.47 |
| | $^{232}$Th | 0.01 |
| | $^{228}$Ra-$^{208}$Pb | 0.16 |
| | $^{235}$U | 0 |
| | $^{129}$I | 1 |
| Quartz | $^{40}$K | 0.495 |
| | $^{238}$U | 12.3 |
| | $^{232}$Th | 4.88 |
| PMTs | $^{40}$K | 9300 |
| | $^{238}$U | 2400 |
| | $^{232}$Th | 1000 |
| Stainless Steel | $^{40}$K | 13.77 |
| | $^{238}$U-$^{230}$Th | 118.31 |
| | $^{226}$Ra-$^{206}$Pb | 2.28 |
| | $^{232}$Th | 6.49 |
| | $^{235}$U | 8.79 |
| | $^{60}$Co | 7.19 |
| Drill Ice | $^{40}$K | 3.71 |
| | $^{60}$Co | 0.12 |
| | $^{238}$U-$^{230}$Th | 6.69 |
| | $^{226}$Ra-$^{206}$Pb | 0.39 |
| | $^{232}$Th | 0.55 |
| | $^{235}$U | 0.38 |
| Copper Case | $^{210}$Pb | 40 mBq |

Table 6.7: Contamination levels of the DM-Ice17 background model. These values describe all the inputs into the simulation of DM-Ice17.

# Chapter 7

# Future Work

The DM-Ice simulation has helped to inform the collaboration in deciding the best way to move forward with the experiment. New crystals have been thoroughly investigated, and several orders put in following measurement of these crystals' contamination. Based on the measurement of the best available contamination of new crystals, and simulation of how this contamination will affect the dark matter search effectiveness, these crystals have been deemed clean enough to perform the measurements we wish to carry out. Two crystals are now running at an underground location at Fermilab (DM-Ice37), for purposes of testing and calibration. Plans are underway for moving forward with a 125-kg detector, likely to be initially deployed at Gran Sasso, with the option to re-deploy at the South Pole after gathering data in Italy for a time.

There is more work to be done with regard to the simulation for DM-Ice. The estimates of contamination derived from comparing simulation to data as described in chapter 6, have fairly high error levels since they were obtained via a fit "by eye." Root contains the functionality to fit the data more specifically, and to tune the simulation to fit the data in a quantifiable fashion. Implementing a method of fitting like this is likely to increase the accuracy of our knowledge of our detectors, and will certainly give a better idea of what the error on those estimates of contamination is. Further work to optimize the design of the full-scale detector is underway. Simulation of a non-ice environment will be essential to optimizing what we can learn from a mine deployment. This is an exciting time for the DM-Ice experiment, and future results will hopefully allow for improved understanding of

direct detection dark matter results in the field, and guide the direction taken by future dark matter experiments.

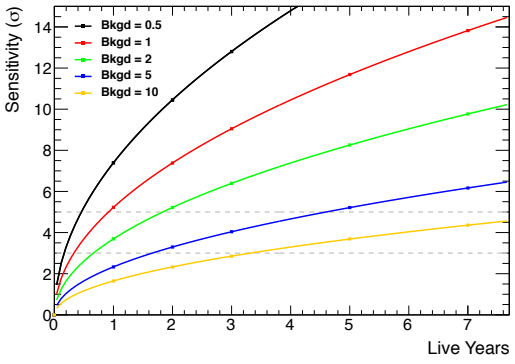


Figure 7.1: Sensitivity for full-scale DM-Ice

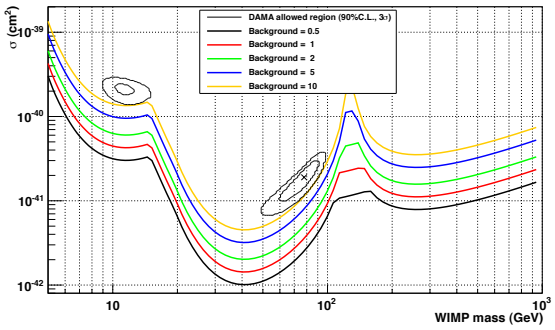


Figure 7.2: Projected exclusion curves for full-scale DM-Ice

The full-scale DM-Ice experiment (see images in Figure 7.3) is moving forward, and currently in the phase of design finalization and component gathering. Projected sensitivity (in case of detection of a modulating signal) and exclusion curves (in case of a null result) can be found in Figures 7.1 and 7.2, respectively.

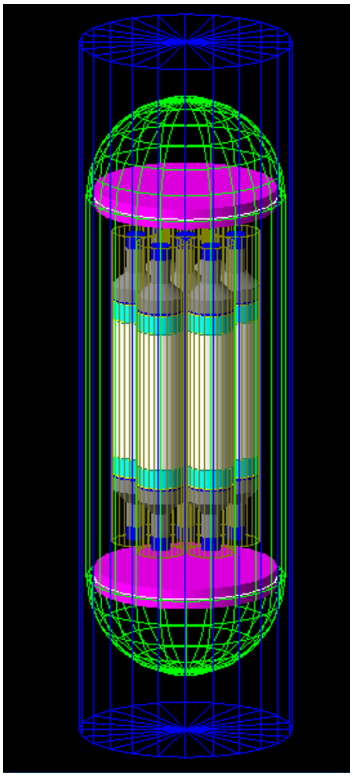

(a)

Simulation visualization

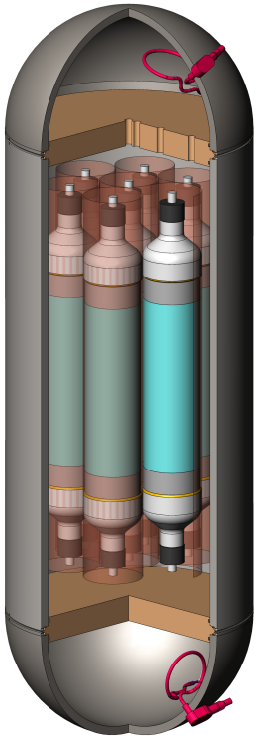

(b)

Engineering drawing

Figure 7.3: Two images of the design of the full scale DM-Ice experiment

# Chapter 8

# Conclusion

The Geant4 simulation of DM-Ice17 has helped us understand our detector's backgrounds. We now have clear estimates on background contamination levels in all components of the detector, as well as its ice surroundings. Simulation has informed which components provide the most background, and which isotopes are of particular concern for future endeavors. The simulation itself is now a robust entity, and protocols exist for performing all parts of simulation setup and analysis, which will be needed by collaboration members as the experiment moves forward. This simulation provides an important reference point on which DM-Ice can base future plans and efforts to understand its detectors.

# LIST OF REFERENCES


[1] P.A.R. Ade et al. Planck 2013 results. XVI. Cosmological parameters. 2013.

[2] ILIAS (integrated large infrastructures for astroparticle science) database on radiopurity of materials.

[3] Ian Lawson and Bruce Cleveland. Low background counting at SNOLAB. *AIP Conf.Proc.*, 1338:68–77, 2011.

[4] R. Bernabei, P. Belli, A. Bussolotti, F. Cappella, R. Cerulli, C. J. Dai, A. D'Angelo, H. L. He, A. Incicchitti, H. H. Kuang, J. M. Ma, A. Mattei, F. Montecchia, F. Nozzoli, D. Prosperi, X. D. Sheng, and Z. P. Ye. The DAMA/LIBRA apparatus. *Nuclear Instruments and Methods in Physics Research A*, 592:297–315, July 2008.

[5] S. Cebrin, C. Cuesta, J. Amar, S. Borjabad, D. Fortuo, E. Garca, C. Ginestra, H. Gmez, M. Martnez, M.A. Olivn, Y. Ortigoza, A. Ortiz de Solrzano, C. Pobes, J. Puimedn, M.L. Sarsa, and J.A. Villar. Background model for a nai (tl) detector devoted to dark matter searches. *Astroparticle Physics*, 37(0):60 – 69, 2012.

[6] K. G. Begeman, A. H. Broeils, and R. H. Sanders. Extended rotation curves of spiral galaxies - Dark haloes and modified dynamics. *Mon. Not. R. Ast.*, 249:523–537, April 1991.

[7] LSST lsst. `http://www.lsst.org/lsst/science/scientist_dark_matter`. Accessed: 2014-07-14.

[8] L. Roszkowski. Particle dark matter - A theorist's perspective. *Pramana*, 62:389, February 2004.

[9] Gianfranco Bertone, editor. *Particle Dark Matter: Observations, Models and Searches*. Cambridge University Press, Cambridge, UK, 2010.

[10] R. Agnese et al. Dark Matter Search Results Using the Silicon Detectors of CDMS II. Technical Report arXiv:1304.4279, Apr 2013.

[11] Robert H. Sanders. *The Dark Matter Problem: A Historical Perspective*. Cambridge University Press, Cambridge, UK, 2010.

[12] LSST Science Collaborations and LSST Project 2009. Lsst science book, version 2.0. 2009.

[13] J. M. Overduin and P. S. Wesson. *Dark Sky, Dark Matter*. Institute of Physics Publishing, Bristol and Philadelphia, 2003.

[14] K. A. Olive, T. Steigman, and T. P. Walker. Primordial Nucleosynthesis: Theory and Observations. *Phys.Rept.*, 333:389–407, 2000.

[15] Andrzej K. Drukier, Katherine Freese, and David N. Spergel. Detecting cold dark-matter candidates. *Phys. Rev. D*, 33:3495–3508, Jun 1986.

[16] Glenn F. Knoll. *Radiation Detection and Measurement*. University of Michigan, Ann Arbor, MI, 2010.

[17] B. Ahmed et al. The NAIAD experiment for WIMP searches at Boulby mine and recent results. *Astroparticle Physics*, 19:691–702, September 2003.

[18] S. C. Kim et al. New Limits on Interactions between Weakly Interacting Massive Particles and Nucleons Obtained with CsI(Tl) Crystal Detectors. 2012.

[19] Yeongduk Kim. KIMS. Dark Matter Silver Jubilee Symposium, PNNL, June 2012.

[20] A. Hime. The MiniCLEAN Dark Matter Experiment. *ArXiv e-prints*, October 2011.

[21] K. Rielage et al. Update on the MiniCLEAN Dark Matter Experiment. *ArXiv e-prints*, March 2014.

[22] P. Gorel. Search for Dark Matter with Liquid Argon and Pulse Shape Discrimination: Results from DEAP-1 and Status of DEAP-3600. *ArXiv e-prints*, June 2014.

[23] G. Angloher et al. Results from 730 kg days of the CRESST-II Dark Matter search. *European Physical Journal C*, 72:1971, April 2012.

[24] K. Heeger et al. The low energy spectrum of $TeO_2$ bolometers: results and dark matter perspectives for the CUORE-0 and CUORE experiments. *Journal of Cosmology and Astroparticle Physics*, 1:38, January 2013.

[25] C. Aalseth et al. Experimental Constraints on a Dark Matter Origin for the DAMA Annual Modulation Effect. *Physical Review Letters*, 101(25):251301, December 2008.

[26] C. Aalseth et al. Search for an Annual Modulation in a p-Type Point Contact Germanium Dark Matter Detector. *Physical Review Letters*, 107(14):141301, September 2011.

[27] C. Aalseth et al. Search for An Annual Modulation in Three Years of CoGeNT Dark Matter Detector Data. *ArXiv e-prints*, January 2014.

[28] R. Bernabei et al. New results from DAMA/LIBRA. *European Physical Journal C*, 67:39–49, May 2010.

[29] R. Bernabei et al. Final model independent result of DAMA/LIBRA-phase1. *European Physical Journal C*, 73:2648, December 2013.

[30] G. Angloher et al. Results on low mass WIMPs using an upgraded CRESST-II detector. *ArXiv e-prints*, July 2014.

[31] K. Blum. DAMA vs. the annually modulated muon background. *ArXiv e-prints*, October 2011.

[32] J. P. Ralston. One Model Explains DAMA/LIBRA, CoGENT, CDMS, and XENON. *ArXiv e-prints*, June 2010.

[33] D. Nygren. A testable conventional hypothesis for the DAMA-LIBRA annual modulation. *ArXiv e-prints*, February 2011.

[34] R. Bernabei, P. Belli, F. Cappella, V. Caracciolo, R. Cerulli, C. J. Dai, A. d'Angelo, A. Di Marco, H. L. He, A. Incicchitti, X. H. Ma, F. Montecchia, X. D. Sheng, R. G. Wang, and Z. P. Ye. No role for muons in the DAMA annual modulation results. *European Physical Journal C*, 72:2064, July 2012.

[35] J. H. Davis. Fitting the annual modulation in DAMA with neutrons from muons and neutrinos. *ArXiv e-prints*, July 2014.

[36] S. Tilav, P. Desiati, T. Kuwabara, D. Rocco, F. Rothmaier, M. Simmons, H. Wissing, and for the IceCube Collaboration. Atmospheric Variations as observed by IceCube. *ArXiv e-prints*, January 2010.

[37] E. Fernandez-Martinez and R. Mahbubani. The Gran Sasso muon puzzle. *Journal of Cosmology and Astroparticle Physics*, 7:29, July 2012.

[38] P. Gabrielli et al. Trace elements in Vostok Antarctic ice during the last four climatic cycles [rapid communication]. *Earth and Planetary Science Letters*, 234:249–259, May 2005.

[39] P. B. Price, K. Woschnagg, and D. Chirkin. Age vs depth of glacial ice at South Pole. *Geophysical Research Letters*, 27:2129–2132, 2000.

[40] DM-Ice Collaboration. First Data from DM-Ice17. *ArXiv e-prints*, January 2014.

[41] Ian Lawson. Slides from Topical Workshop in Low Radioactivity Techniques (Sudbury, Canada): http://www.snolab.ca/lrt2010/talks/Session3/lrt˙2010˙Ian˙Lawson.pdf, August 2010.